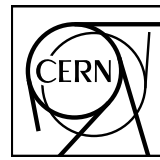


# EUROPEAN ORGANIZATION FOR NUCLEAR RESEARCH



CERN-EP-2019 -XXX  
Day Month 2019

## $\Lambda K$ femtoscopy in Pb-Pb collisions at $\sqrt{s_{NN}} = 2.76$ TeV

ALICE Collaboration\*

### Abstract

We present the first measurement of the scattering parameters of  $\Lambda K$  pairs in all three charge combinations ( $\Lambda K^+$ ,  $\Lambda K^-$ , and  $\Lambda K_S^0$ ). We achieve the measurements through our femtoscopic analysis of  $\Lambda K$  correlations in Pb-Pb collisions at  $\sqrt{s_{NN}} = 2.76$  TeV from ALICE. The femtoscopic correlations result from strong final-state interactions, and are fit with a parametrization allowing us to both characterize the pair emission source and measure the scattering parameters for the particle pairs. We perform an extensive study with the THERMINATOR 2 event generator to account for both non-femtoscopic backgrounds, as well as contributions from residual correlations induced by feed-down from resonances. We find the non-femtoscopic background is due almost entirely to collective effects, and we are able to use the event generator to quantitatively describe it with unprecedented precision. In the experimental data, we observe a striking difference between the  $\Lambda K^+$  and  $\Lambda K^-$  correlations in pairs with low relative momenta ( $k^* \lesssim 100$  MeV). The  $\Lambda K^+$  system exhibits a negative real component of the scattering parameter ( $\Re f_0$ ), while that of the  $\Lambda K^-$  is positive. The underlying cause dictating this interesting difference in the strong force between the two systems is not completely understood. The results might suggest an effect arising from different quark-antiquark interactions between the pairs ( $s\bar{s}$  in  $\Lambda K^+$  and  $u\bar{u}$  in  $\Lambda K^-$ ), or from different net strangeness for each system ( $S=0$  for  $\Lambda K^+$ , and  $S=-2$  for  $\Lambda K^-$ ). Finally, we find that the  $\Lambda K$  systems exhibit source radii larger than expected from extrapolation from identical particle femtoscopic studies. We understand this effect to result from the separation in space-time of the single-particle  $\Lambda$  and  $K$  source distributions.

© 2019 CERN for the benefit of the ALICE Collaboration.

Reproduction of this article or parts of it is allowed as specified in the CC-BY-4.0 license.

\*See Appendix F for the list of collaboration members

## 24 1 Introduction

25 Femtoscopy is an experimental method used to study the space-time characteristic of the particle emitting  
 26 sources in relativistic particle collisions [1]. With this method, two(or many)-particle relative-momentum  
 27 correlation functions are used to connect the final-state momentum distributions to the space-time distri-  
 28 butions of particle emission at freeze-out. The correlation functions are sensitive to quantum statistics, as  
 29 well as strong and Coulomb final-state interactions (FSI). In addition to characterizing the source region,  
 30 femtoscopy offers a unique opportunity to measure nuclear scattering parameters, many of which are  
 31 difficult, if not impossible, to measure otherwise. In many pair systems, the contributions to the cor-  
 32 relation function from quantum statistics and/or the Coulomb interaction overwhelm that of the strong  
 33 interaction, making it difficult to extract scattering information. In this article, we study non-identical  
 34 particle pairs, with at least one electrically neutral particle in the pair. Therefore, quantum statistics and  
 35 the Coulomb interaction do not contribute, giving us a clear signal from the strong interaction.

36 Femtoscopic analyses of pion, kaons, and protons have revealed a trend of decreasing source radii with  
 37 increasing transverse mass [2], which, for identical particle pairs, is defined as  $m_T^2 = m^2 + k_T^2$ , where  
 38  $k_T = \frac{1}{2}|\mathbf{p}_{T,1} + \mathbf{p}_{T,2}|$ . This is interpreted as a signature of hydrodynamic flow, and therefore deconfined  
 39 quark matter, in the heavy-ion collisions [3]. The exponent for  $m_T$ -scaling can be shown analytically to  
 40 be  $-\frac{1}{2}$  for case of a one-dimensional longitudinal hydrodynamic expansion with negligible transverse  
 41 flow and common freeze-out characteristics, regardless of particle species. This has lead to an idea  
 42 of universal  $m_T$ -scaling for different particle species. However, it is unclear how picture changes with  
 43 significant transverse flow, viscosity corrections, and hadronic rescattering. Additionally, the scaling  
 44 observed in models exists separately for the three-dimensional radii in the Longitudinally Co-Moving  
 45 System (LCMS), and will at best only be approximate in the Pair Rest Frame (PRF) [2, 4].

46 The radii we extract from our study are larger than one would expect from naively following the trends  
 47 set forth in the identical particle analyses. However, when dealing with non-identical particles, such  
 48 as in the present case with ΛK pairs, we should not necessarily expect the exact same trend. In such  
 49 cases, the pair emission source, measured through femtoscopy, is the superposition of two single-particle  
 50 sources, each with its own unique size, shape, and space-time position within the medium. Although the  
 51 single-particle sources should abide by the approximate  $m_T$ -scaling, the pair sources generally will not.

52 This paper presents the first measurement of the scattering parameters of ΛK pairs in all three charge  
 53 combinations ( $\Lambda K^+$ ,  $\Lambda K^-$ , and  $\Lambda K_S^0$ ). The scattering parameters, along with pair emission source sizes,  
 54 are extracted with a femtoscopic analysis of ΛK correlations in Pb-Pb collisions at  $\sqrt{s_{NN}} = 2.76$  TeV  
 55 from ALICE experiment at the LHC. These correlations result from strong final-state interactions, and  
 56 are fit with a parametrization by Lednicky and Lyuboshitz [5]. We perform an extensive study with the  
 57 THERMINATOR 2 event generator to account for both non-femtoscopic backgrounds, as well as contribu-  
 58 tions from residual correlations induced by feed-down from resonances. We find the non-femtoscopic  
 59 background is due almost entirely to collective effects, and we are able to use the event generator to  
 60 quantitatively describe it with unprecedented precision. In the experimental data, we observe a striking  
 61 difference between the  $\Lambda K^+$  and  $\Lambda K^-$  correlations in pairs with low relative momenta ( $k^* \lesssim 100$  MeV).  
 62 The  $\Lambda K^+$  system exhibits a negative real component of the scattering parameter ( $\Re f_0$ ), while that of the  
 63  $\Lambda K^-$  is positive. The underlying cause dictating this interesting difference in the strong force between  
 64 the two systems is not completely understood. The results might suggest an effect arising from differ-  
 65 ent quark-antiquark interactions between the pairs ( $s\bar{s}$  in  $\Lambda K^+$  and  $u\bar{u}$  in  $\Lambda K^-$ ), or from different net  
 66 strangeness for each system ( $S = 0$  for  $\Lambda K^+$ , and  $S = -2$  for  $\Lambda K^-$ ). Finally, we find that the ΛK systems  
 67 exhibit source radii larger than expected from extrapolation from identical particle femtoscopic studies.  
 68 We understand this effect to be result from the separation in space-time of the single-particle Λ and K  
 69 distributions. For the study of ΛK pairs at mid-rapidity in Pb-Pb collisions, we expect a separation of the  
 70 single-particle sources in the out direction. The effect of a non-zero shift in the source will naturally lead  
 71 to larger measured radii.

- 72 Note, we expect and observe consistent results between a particle pair and its conjugate (ex.  $\Lambda K^+$  and  
 73  $\bar{\Lambda} K^-$ ); therefore, we group the two together as a single analysis by fitting them simultaneously with  
 74 a shared parameter set, and will refer to the joined analysis simply by the pair name, excluding the  
 75 conjugate. So, for instance,  $\Lambda K_S^0 \oplus \bar{\Lambda} K_S^0$  is simply  $\Lambda K_S^0$ ,  $\Lambda K^+ \oplus \bar{\Lambda} K^-$  is  $\Lambda K^+$ , etc.
- 76 The organization of this paper is as follows. In Sec. 2 we discuss briefly our methods for selecting the  
 77 data. In Sec. 3 we present our analysis technique. We introduce the two particle correlation function, as  
 78 well as the theoretical models with which we fit. This section also includes descriptions of our handling  
 79 of residual correlations, corrections accounting for finite track momentum resolution, treatment of the  
 80 non-femtoscopic background, as well as a brief description of our estimation systematic uncertainties.  
 81 Our results are presented in Sec. 4, and concluding remarks are given in Sec. 5.

## 82 2 Data Analysis

83 The dataset analyzed is from Pb-Pb collisions at  $\sqrt{s_{NN}} = 2.76$  TeV at the LHC measured by the ALICE  
 84 detector [6]. Approximately 40 million combined central, semi-central, and minimum bias events were  
 85 analyzed. The events were classified according to their centrality determined using the measured ampli-  
 86 tudes in the V0 detectors [7]. In order for an event to be included in the analysis, the z-position of the  
 87 reconstructed event vertex must be within 10 cm of the center of the ALICE detector, and the event must  
 88 contain at least one particle of each type from the pair of interest (ex. for  $\Lambda K_S^0$  analysis, an accepted  
 89 event must contain at least one  $\Lambda$  and at least one  $K_S^0$ ).

90 Charged particle tracking was performed using the Time Projection Chamber (TPC) [8] and the Inner  
 91 Tracking System [6]. The ITS allows for high spatial resolution in determining the primary (collision)  
 92 vertex. The determination of the momenta of the tracks was performed using tracks reconstructed with  
 93 the TPC only and constrained to the primary vertex. A minimum requirement on the number of recon-  
 94 structed TPC clusters was imposed, the purpose of which is to ensure both the quality of the track and  
 95 good  $p_T$  resolution at large momenta, as well as to remove fake tracks.

96 Particle identification (PID) for reconstructed tracks was carried out using both the TPC and Time-of-  
 97 Flight (TOF) detector [9, 10] in the pseudorapidity range  $|\eta| < 0.8$ . For TPC PID, a parametrized  
 98 Bethe-Bloch formula was used to calculate the specific energy loss  $\langle dE/dx \rangle$  in the detector expected  
 99 for a particle with a given mass and momentum. For TOF PID, the particle mass was used to calculate  
 100 the expected time-of-flight as a function of track length and momentum. For each PID method, a value  
 101 ( $N\sigma$ ) was assigned to each track denoting the number of standard deviations between the measured track  
 102 information and calculated values. This procedure was repeated for four “particle species hypotheses”  
 103 - electron, pion, kaon, and proton-, and, for each hypothesis, a different  $N\sigma$  value was obtained per  
 104 detector.

### 105 2.1 $K^\pm$ selection

106 The single-particle selection criteria used to select charged kaon candidates are summarized in Table 1.  
 107  $K^\pm$  track detection utilized both TPC and TOF detectors, and tracks within the range  $0.14 < p_T < 1.5$   
 108 GeV/c were accepted. As we are interested in primary particles originating from the primary vertex,  
 109 to reduce the number of secondaries (for instance, charged particles produced in the detector material,  
 110 particles from weak decays, etc.) in our sample, we established a maximum cut on the distance-of-  
 111 closest-approach (DCA) of the track to the primary vertex. This restriction is realized by imposing a  
 112 DCA cut in both the transverse and beam directions.

113 PID was performed using both the TPC and TOF detectors via the  $N\sigma$  method. Additionally, we include  
 114 methods to reduce the contamination in our  $K^\pm$  samples from electrons and pions. The specifics for these  
 115 cuts are contained in Table 1.

<b>K<sup>±</sup> selection</b>	
Transverse momentum $p_T$	$0.14 < p_T < 1.5 \text{ GeV}/c$
$ \eta $	$< 0.8$
Transverse DCA to primary vertex	$< 2.4 \text{ cm}$
Longitudinal DCA to primary vertex	$< 3.0 \text{ cm}$
TPC and TOF N $\sigma$ Cuts	
$p < 0.4 \text{ GeV}/c$	$N_{\sigma K, \text{TPC}} < 2$
$0.4 < p < 0.45 \text{ GeV}/c$	$N_{\sigma K, \text{TPC}} < 1$
$0.45 < p < 0.80 \text{ GeV}/c$	$N_{\sigma K, \text{TPC}} < 3$ $N_{\sigma K, \text{TOF}} < 2$
$0.80 < p < 1.0 \text{ GeV}/c$	$N_{\sigma K, \text{TPC}} < 3$ $N_{\sigma K, \text{TOF}} < 1.5$
$p > 1.0 \text{ GeV}/c$	$N_{\sigma K, \text{TPC}} < 3$ $N_{\sigma K, \text{TOF}} < 1$
Electron Rejection: Reject if all satisfied	$N_{\sigma e^-, \text{TPC}} < 3$ $N_{\sigma e^-, \text{TPC}} < N_{\sigma K^\pm, \text{TPC}}$ $N_{\sigma e^-, \text{TOF}} < N_{\sigma K^\pm, \text{TOF}}$
Pion Rejection: Reject if:	
	TOF and TPC available
$p < 0.65 \text{ GeV}/c$	$N_{\sigma \pi, \text{TPC}} < 3$ $N_{\sigma \pi, \text{TOF}} < 3$
	Only TPC available
	$p < 0.5 \text{ GeV}/c$
	$N_{\sigma \pi, \text{TPC}} < 3$
	$0.5 < p < 0.65 \text{ GeV}/c$
	$N_{\sigma \pi, \text{TPC}} < 2$
$0.65 < p < 1.5 \text{ GeV}/c$	$N_{\sigma \pi, \text{TPC}} < 5$ $N_{\sigma \pi, \text{TOF}} < 3$
$p > 1.5 \text{ GeV}/c$	$N_{\sigma \pi, \text{TPC}} < 5$ $N_{\sigma \pi, \text{TOF}} < 2$

**Table 1:** K<sup>±</sup> selection

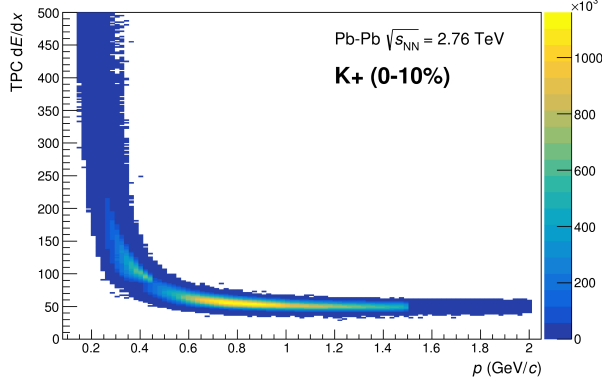


**Fig. 1:** Sample  $dE/dx$  distribution for the  $K^+$  collection from our 0-10% central  $\Lambda K^+$  analysis.

116 The purity of the  $K^\pm$  collections was estimated from a Monte-Carlo (MC) study based on HIJING [11]  
 117 simulations using GEANT3 [12] to model particle transport through the ALICE detectors. In these  
 118 simulations, the true identity of each reconstructed  $K^\pm$  particle is known; therefore, the purity may be  
 119 estimated as:

$$\text{Purity}(K^\pm) = \frac{N_{\text{true}}}{N_{\text{reconstructed}}} \quad (1)$$

120 For our analysis, we find  $\text{Purity}(K^+) \approx \text{Purity}(K^-) \approx 97\%$ . Figure 1 shows a sample  $dE/dx$  for the  $K^+$   
 121 collection in the 0-10% centrality bin (from our  $\Lambda K^+$  study).

## 122 2.2 V0 selection

123  $\Lambda(\bar{\Lambda})$  and  $K_S^0$  particles are electrically neutral, and cannot be directly detected, but must instead be re-  
 124 constructed through detection of their decay products, or daughters. This process is illustrated in Figure  
 125 2, and the main cuts used are shown in Tables 2 and 3. In general, particles which are topologically  
 126 reconstructed in this fashion are called V0 particles. The decay channel  $\Lambda \rightarrow p\pi^-$  was used for the  
 127 identification of  $\Lambda$  hyperons (and, similarly the charge-conjugate decay for the  $\bar{\Lambda}$  identification), and  $K_S^0$   
 128  $\rightarrow \pi^+\pi^-$  for the identification of  $K_S^0$  mesons.

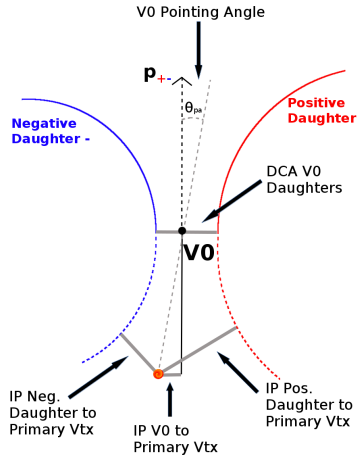


**Fig. 2:** V0 Reconstruction

129 To construct a V0 particle, the charged daughter tracks must first be found. Aside from typical kinematic  
 130 and PID cuts (using TPC and TOF detectors), the daughter tracks are also exposed to a minimum cut

on their impact parameter with respect to the primary vertex. The daughters of a V0 particle should not originate from the primary vertex, but rather from the decay vertex of the V0, hence the minimum cut imposition. The decay vertex of the V0 is assumed to be the point of closest approach between the daughter tracks. To help ensure quality, a maximum value cut is demanded on the distance-of-closest-approach between the daughters (DCA V0 Daughters). The positive and negative daughter tracks are combined to form the V0 candidate, the momentum of which is simply the sum of the momenta of the daughters (calculated at the DCA).

A minimum transverse momentum cut on the V0 candidate is introduced to reduce contamination from fake candidates. Opposite to that of the daughter tracks, the V0 candidate is exposed to a maximum cut on its impact parameter with respect to the primary vertex. In this case, we do want our V0 candidates to be primary, hence the maximum cut imposition. To further strengthen our selection of primary V0 candidates, we impose a selection on the pointing angle,  $\theta_{\text{pa}}$ , between the V0 momentum and the vector pointing from the primary vertex to the secondary V0 decay vertex. We want the V0 candidate's momentum to point back to the primary decay vertex, and therefore a small  $\theta_{\text{pa}}$ ; we achieve this by appointing a minimum value on  $\cos(\theta_{\text{pa}})$  (“Cosine of pointing angle” in Tables 2 and 3).

On occasion,  $\Lambda(\bar{\Lambda})$  particles are misidentified as  $K_S^0$ , and vice versa. To attempt to remove these contaminations without throwing away good candidates, we impose a set of misidentification cuts. The intent of these cuts is to judge whether a candidate is more likely a  $\Lambda(\bar{\Lambda})$  or a  $K_S^0$ , and are implemented as described below. For a given V0, we calculate the mass assuming different identities ( $\Lambda$ ,  $\bar{\Lambda}$ ,  $K_S^0$ ) of the candidate; the mass assuming  $K_S^0$  hypothesis ( $m_{\text{inv}, K_S^0 \text{ hyp.}}$ ) is calculated assuming  $\pi^+\pi^-$  daughters, the mass assuming  $\Lambda$  hypothesis ( $m_{\text{inv}, \Lambda \text{ hyp.}}$ ) is calculated assuming  $p\pi^-$  daughters, and the mass assuming  $\bar{\Lambda}$  hypothesis ( $m_{\text{inv}, \bar{\Lambda} \text{ hyp.}}$ ) is calculated assuming  $\bar{p}\pi^+$  daughters. In addition to the notation just introduced, in the following,  $m_{\text{PDG}, K_S^0}$  and  $m_{\text{PDG}, \Lambda(\bar{\Lambda})}$  denote the particle masses of the  $K_S^0$  and  $\Lambda(\bar{\Lambda})$ , respectively, as recorded by the Particle Data Group [13].

For  $\Lambda(\bar{\Lambda})$  selection, a candidate is assumed to be misidentified and is rejected if all of the following criteria are satisfied:

$$1. \left| m_{\text{inv}, K_S^0 \text{ hyp.}} - m_{\text{PDG}, K_S^0} \right| < 9.0 \text{ MeV}/c^2$$

2. The daughter particles pass daughter cuts intended for  $K_S^0$  reconstruction

(a)  $\Lambda$  selection

- i. p daughter passes  $\pi^+$  cuts intended for  $K_S^0$  reconstruction
- ii.  $\pi^-$  daughter passes  $\pi^-$  cuts intended for  $K_S^0$  reconstruction.

(b)  $\bar{\Lambda}$  selection

- i.  $\pi^+$  daughter passes  $\pi^+$  cuts intended for  $K_S^0$  reconstruction
- ii.  $\bar{p}$  daughter passes  $\pi^-$  cuts intended for  $K_S^0$  reconstruction.

$$3. \left| m_{\text{inv}, K_S^0 \text{ hyp.}} - m_{\text{PDG}, K_S^0} \right| < \left| m_{\text{inv}, \Lambda(\bar{\Lambda}) \text{ hyp.}} - m_{\text{PDG}, \Lambda(\bar{\Lambda})} \right|$$

Similarly, for  $K_S^0$  selection, a candidate is rejected if all of the following criteria are satisfied for the  $\Lambda$  case, or for the  $\bar{\Lambda}$  case:

$$1. \left| m_{\text{inv}, \Lambda(\bar{\Lambda}) \text{ hyp.}} - m_{\text{PDG}, \Lambda(\bar{\Lambda})} \right| < 9.0 \text{ MeV}/c^2$$

2. The daughter particles pass daughter cuts intended for  $\Lambda(\bar{\Lambda})$  reconstruction

- 170 (a)  $\pi^+$  daughter passes  $p(\pi^+)$  daughter cut intended for  $\Lambda(\bar{\Lambda})$  reconstruction  
 171 (b)  $\pi^-$  daughter passes  $\pi^-(\bar{p})$

172 3.  $|m_{\text{inv}, \Lambda(\bar{\Lambda}) \text{ hyp.}} - m_{\text{PDG}, \Lambda(\bar{\Lambda})}| < |m_{\text{inv}, K_S^0 \text{ hyp.}} - m_{\text{PDG}, K_S^0}|$

173 At this stage, we have a collection of V0 candidates satisfying all of the aforementioned cuts. However,  
 174 this collection is still polluted by fake V0s, for which the daughter particles happen to pass all of our cuts,  
 175 but which do not actually originate from a V0. Although the two daughter particles appear to reconstruct  
 176 a V0 candidate, they are lacking one critical requirement: the system invariant mass does not match that  
 177 of our desired V0 species (these can be seen outside of the mass peaks in Fig. 3). Therefore, as our final  
 178 single-particle cut, we require the invariant mass of the V0 candidate to fall within the mass peak of our  
 179 desired species. Note, however, that some fake V0s still make it past this final cut, as their invariant mass  
 180 also happens to fall without our acceptance window.

<b>Λ selection</b>	
Transverse momentum $p_T$	$> 0.4 \text{ GeV}/c$
$ \eta $	$< 0.8$
$ m_{\text{inv}} - m_{\text{PDG}} $	$< 3.8 \text{ MeV}$
DCA to primary vertex	$< 0.5 \text{ cm}$
Cosine of pointing angle	$> 0.9993$
Decay Length	$< 60 \text{ cm}$
<b>Daughter Cuts (<math>\pi</math> and <math>p</math>)</b>	
$ \eta $	$< 0.8$
DCA $\pi p$ Daughters	$< 0.4 \text{ cm}$
<b><math>\pi</math>-specific cuts</b>	
$p_T$	$> 0.16 \text{ GeV}/c$
DCA to primary vertex	$> 0.3 \text{ cm}$
<b>TPC and TOF <math>N\sigma</math> Cuts</b>	
$p < 0.5 \text{ GeV}/c$	$N\sigma_{\text{TPC}} < 3$
$p > 0.5 \text{ GeV}/c$	$N\sigma_{\text{TPC}} < 3$
	$N\sigma_{\text{TOF}} < 3$
TOF & TPC available	$N\sigma_{\text{TPC}} < 3$
Only TPC available	$N\sigma_{\text{TPC}} < 3$
<b><math>p</math>-specific cuts</b>	
$p_T$	$> 0.5(p) [0.3(\bar{p})] \text{ GeV}/c$
DCA to primary vertex	$> 0.1 \text{ cm}$
<b>TPC and TOF <math>N\sigma</math> Cuts</b>	
$p < 0.8 \text{ GeV}/c$	$N\sigma_{\text{TPC}} < 3$
$p > 0.8 \text{ GeV}/c$	$N\sigma_{\text{TPC}} < 3$
	$N\sigma_{\text{TOF}} < 3$
TOF & TPC available	$N\sigma_{\text{TPC}} < 3$
Only TPC available	$N\sigma_{\text{TPC}} < 3$

**Table 2:** Λ selection

181 Occasionally, we encounter a situation where two V0 candidates share a common daughter. Not both of  
 182 these candidates can be real V0s, and including both could introduce an artificial signal into our data.  
 183 To avoid any auto-correlation effects, for each event, we impose a single-particle shared daughter cut on  
 184 each collection of V0 candidates. This cut iterates through the V0 collection to ensure that no daughter is  
 185 claimed by more than one V0 candidate. If a shared daughter is found between two V0 candidates, that  
 186 candidate with a smaller DCA to primary vertex is kept while the other is excluded from the analysis.  
 187 Note, this single-particle shared daughter cut is unique from the pair shared daughter cut discussed in  
 188 Sec. 2.3, the latter of which ensure there is no daughter sharing between the particles in a given pair.

<b><math>K_S^0</math> selection</b>					
Transverse momentum $p_T$	$> 0.2 \text{ GeV}/c$				
$ \eta $	$< 0.8$				
$m_{PDG} - 13.677 \text{ MeV} < m_{\text{inv}} < m_{PDG} + 2.0323 \text{ MeV}$					
DCA to primary vertex	$< 0.3 \text{ cm}$				
Cosine of pointing angle	$> 0.9993$				
Decay Length	$< 30 \text{ cm}$				
<b><math>\pi^\pm</math> Daughter Cuts</b>					
$p_T$	$> 0.15 \text{ GeV}/c$				
$ \eta $	$< 0.8$				
DCA $\pi^+ \pi^-$ Daughters	$< 0.3 \text{ cm}$				
DCA to primary vertex	$> 0.3 \text{ cm}$				
TPC and TOF $N\sigma$ Cuts					
$p < 0.5 \text{ GeV}/c$	$N\sigma_{\text{TPC}} < 3$				
$p > 0.5 \text{ GeV}/c$	<table border="1"> <tr> <td>TOF &amp; TPC available</td><td><math>N\sigma_{\text{TPC}} &lt; 3</math></td></tr> <tr> <td>Only TPC available</td><td><math>N\sigma_{\text{TOF}} &lt; 3</math></td></tr> </table>	TOF & TPC available	$N\sigma_{\text{TPC}} < 3$	Only TPC available	$N\sigma_{\text{TOF}} < 3$
TOF & TPC available	$N\sigma_{\text{TPC}} < 3$				
Only TPC available	$N\sigma_{\text{TOF}} < 3$				
	$N\sigma_{\text{TPC}} < 3$				

**Table 3:**  $K_S^0$  selection

189 In order to obtain a true and reliable signal, one must ensure good purity of the V0 collection. The purity  
 190 of the collection is calculated as:

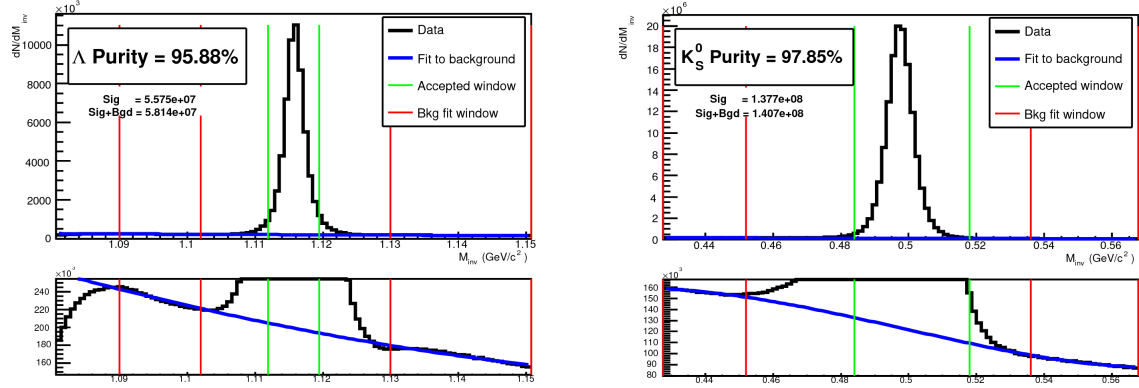
$$\text{Purity} = \frac{\text{Signal}}{\text{Signal} + \text{Background}} \quad (2)$$

191 To access both the signal and background, the invariant mass distribution ( $m_{\text{inv}}$ ) of all V0 candidates  
 192 must be constructed immediately before the final invariant mass cut, as shown in Fig. 3 for  $\Lambda$  and  $K_S^0$   
 193 candidates in the 0-10% centrality bin. Figure 3(a) presents the  $p\pi^-$  invariant mass distribution showing  
 194 the  $\Lambda$  peak, and Figure 3(b) presents the  $\pi^+ \pi^-$  invariant mass distribution showing the  $K_S^0$  peak. It is  
 195 vital that this distribution be constructed immediately before the final  $m_{\text{inv}}$  cut, otherwise it would be  
 196 impossible to estimate the background. These distributions (and similar for  $\bar{\Lambda}$ ) are used to calculate the  
 197 collections' purities (defined in Eq. 2). As shown in Figure 3, the background is fit (with a polynomial)  
 198 outside of the peak region of interest to obtain an estimate for the background within the region. Within  
 199 the  $m_{\text{inv}}$  cut limits, the background is assumed to be the region below the fit while the signal is that above  
 200 the fit. The  $\Lambda$  and  $\bar{\Lambda}$  purities were found to be  $\approx 95\%$ , and the  $K_S^0$  purity was found to be  $\approx 98\%$ .

### 201 2.3 Pair Construction

202 The femtoscopic analysis of two-particle correlation functions relies on the proper formation of particle  
 203 pairs. As such, it is important to obtain true particle pairs in the analysis. In particular, contamination  
 204 from pairs constructed with split or merged tracks, and pairs sharing daughters, can introduce artificial  
 205 signals into the correlation function, obscuring the actual physics. In an effort to remove contamination,  
 206 we impose two main pair cuts: a shared daughter cut, and an average separation cut.

207 The purpose of the shared daughter cut is to ensure the first particle in the pair is unique from the second.  
 208 For pairs formed of two V0s (i.e.  $\Lambda K_S^0$ ), this cut is implemented by removing all pairs which share a  
 209 daughter (ex. in  $\Lambda K_S^0$  analysis, if the  $\Lambda$  and  $K_S^0$  in a potential pair claim the same  $\pi^-$  daughter, the pair  
 210 is excluded from the analysis). For a pair formed of a single V0 and a charged track (i.e.  $\Lambda K^\pm$ ), the cut  
 211 removes all pairs in which the charged track is also claimed as a daughter of the V0. This mistake could  
 212 only occur if, for instance, either a  $K^\pm$  is misidentified as a  $\pi$  or p in the V0 reconstruction, or a  $\pi$  or p is  
 213 misidentified as a  $K^\pm$  in the  $K^\pm$  selection.



(a)  $p\pi^+$  invariant mass distribution where the  $\Lambda$  peak is seen. (b)  $\pi^+\pi^-$  invariant mass distribution where the  $K_S^0$  peak is seen.

**Fig. 3:** Invariant mass ( $m_{\text{inv}}$ ) distribution of  $p\pi^+$  pairs showing the  $\Lambda$  peak 3(a), and of  $\pi^+\pi^-$  pairs showing the  $K_S^0$  peak 3(b), for V0 candidates immediately before the final invariant mass cut (for the 0-10% centrality bin). The bottom panels are zoomed to show the background with fit. The vertical green lines represent the  $m_{\text{inv}}$  cuts used in the analyses, the red vertical lines delineate the region over which the background was fit, and the blue line shows the background fit. These distributions (and similar, for  $\bar{\Lambda}$ ) are used to calculate the collection purities,  $\text{Purity}(\Lambda) \approx \text{Purity}(\bar{\Lambda}) \approx 95\%$ , and  $\text{Purity}(K_S^0) \approx 98\%$ .

214 The purpose of the average separation cut is to remove splitting and merging effects, and it is employed  
 215 in the following way. To calculate the average separation between two tracks, the spatial separation is  
 216 determined at several points throughout the TPC (every 20 cm radially from 85 cm to 245 cm), and the  
 217 results averaged. For that  $\Lambda K_S^0$  analysis, which involves two V0 particles, a minimum average separation  
 218 cut of 6 cm between the like-charge daughters in the pairs was imposed (for example, between the  $p$   
 219 daughter of the  $\Lambda$  and the  $\pi^+$  daughter of the  $K_S^0$ ). For the  $\Lambda K^\pm$  analyses, a minimum average separation  
 220 cut of 8 cm was enforced between the  $K^\pm$  and the  $\Lambda$  daughter sharing the same charge (for example, in the  
 221  $\Lambda K^+$  analysis, between the  $p$  daughter of the  $\Lambda$  and the  $K^+$ ). The values used in these cuts were obtained  
 222 by first forming average separation correlation functions. This is done just as for our relative-momentum  
 223 correlation functions, but we instead bin in average separation. Looking at these average separation  
 224 correlation functions for like-charge tracks, at lowest average separation we see an enhancement due to  
 225 track splitting, followed by (at slightly higher average separation) a suppression due to track merging.  
 226 When the average separation correlation function stabilizes to unity, these effects are no longer abundant,  
 227 and we choose our cut value. Splitting and merging effects between oppositely charged tracks was found  
 228 to be negligible, therefore no cuts on unlike-charge tracks were imposed.

### 229 3 Analysis Methods

#### 230 3.1 Correlation Function

231 Two-particle correlation functions are built as the ratio of the covariant two-particle and single-particle  
 232 spectra:

$$C^{ab}(\vec{p}_a, \vec{p}_b) = \frac{E_a E_b \frac{dN^{ab}}{d^3 p_a d^3 p_b}}{(E_a \frac{dN^a}{d^3 p_a})(E_b \frac{dN^b}{d^3 p_b})} \quad (3)$$

233 This may be expressed theoretically as in the Koonin-Pratt equation [14, 15]:

$$C(\mathbf{k}^*) = \int S_{\mathbf{P}}(\mathbf{r}^*) |\Psi_{\mathbf{k}^*}(\mathbf{r}^*)|^2 d^3\mathbf{r}^* \quad (4)$$

234 where  $\mathbf{k}^*$  and  $\mathbf{r}^*$  are the relative momentum and separation in the pair rest frame,  $\mathbf{P}$  is the total pair  
 235 momentum,  $S_{\mathbf{P}}(\mathbf{r}^*)$  is the pair source distribution, and  $\Psi_{\mathbf{k}^*}(\mathbf{r}^*)$  is the two-particle wave-function. Within  
 236 the  $|\Psi|^2$  term is contained the particle interaction information, and therefore the scattering parameters.  
 237 Equation 4 reveals the limitations of femtoscopy; at best, we are able to probe the distribution of relative  
 238 positions of particles with identical velocities and total momentum  $\mathbf{P}$  as they move in an asymptotic state.  
 239 Therefore, we do not measure the entire size of the source, but rather the “regions of homogeneity” [3].

240 In practice, the correlation function is formed experimentally as:

$$C(k^*) = \mathcal{N} \frac{A(k^*)}{B(k^*)} \quad (5)$$

241 where  $A(k^*)$  is the signal distribution,  $B(k^*)$  is the reference distribution, and  $\mathcal{N}$  is a normalization  
 242 parameter.  $B(k^*)$  is used to divide out the phase-space effects, leaving only the femtoscopic effects in the  
 243 correlation function. The normalization parameter is chosen such that the mean value of the correlation  
 244 function equal unity for  $k^* \in [0.32, 0.4] \text{ GeV}/c$ .

245 In practice,  $A(k^*)$  is constructed by binning in  $k^*$  pairs from the same event. Ideally,  $B(k^*)$  is similar to  
 246  $A(k^*)$  in all respects excluding the presence of femtoscopic correlations [1]. Typically,  $B(k^*)$  is obtained  
 247 by forming mixed-event pairs, i.e. particles from a given event are paired with particles from  $N_{\text{mix}}$   
 248 other events, and these pairs are then binned in  $k^*$ . Other techniques exist; most notably, one may use  
 249 same-event pairs after rotating one particle in the pair by  $180^\circ$  in the transverse plane (see Sec. 3.5  
 250 and App. B for more details). However, for this analysis, we use the typical mixed-event method. In  
 251 forming the reference distribution, it is important to mix only similar events; mixing events with different  
 252 phase-spaces can result in an unreliable reference, and can introduce artificial signals in the correlation  
 253 function. Therefore, in this analysis, we bin our events both in primary vertex location (2 cm bin width)  
 254 and in centrality (5% bin width), and we only mix events within a given bin; i.e. we only mix events  
 255 of like centrality and of like primary vertex location. Additionally, we use  $N_{\text{mix}} = 5$  as the size of our  
 256 mixing pool. Also note, a vertex correction is also applied to each event, which essentially recenters the  
 257 the primary vertices to  $z = 0$ .

258 This analysis presents correlation functions for three centrality bins (0-10%, 10-30%, and 30-50%), and  
 259 is currently pair transverse momentum ( $k_T = \frac{1}{2} |\mathbf{p}_{T,1} + \mathbf{p}_{T,2}|$ ) integrated (i.e. not binned in  $k_T$ ). The  
 260 correlation functions are constructed separately for the two magnetic field configurations (++ and - -),  
 261 and are combined using a weighted average:

$$C(k^*) = \frac{\sum_i w_i C_i(k^*)}{\sum_i w_i} \quad (6)$$

262 where the sum runs over the correlation functions to be combined, and the weight,  $w_i$ , is the number of  
 263 numerator pairs in the normalization range for  $C_i(k^*)$ .

### 264 3.2 Modeling the correlation function

265 In the absence of the Coulomb interaction, the correlation function can be described analytically with a  
 266 model derived by Lednický and Lyuboshitz [5]. Within the model, the (non-symmetrized) two-particle  
 267 wave function is expressed as a superposition of a plane wave and diverging spherical wave:

$$\Psi^S(\mathbf{k}^*, \mathbf{r}^*) = e^{-i\mathbf{k}^* \cdot \mathbf{r}^*} + f^S(k^*) \frac{e^{ik^* r^*}}{r^*} \quad (7)$$

268 In the effective range approximation, the complex s-wave scattering amplitude,  $f^S(k^*)$ , with  $S$  denoting  
 269 the total spin of the particular pair, is of the form

$$f^S(k^*) = \left( \frac{1}{f_0^S} + \frac{1}{2} d_0^S k^{*2} - ik^* \right)^{-1} \quad (8)$$

270 where  $f_0^S$  is the complex s-wave scattering length, and  $d_0^S$  is the effective range of the interaction. A  
 271 spherically symmetric Gaussian distribution is assumed for the pair emission source in the PRF

$$S(\mathbf{r}^*) \propto \exp \left[ -\frac{r^{*2}}{4R_{\text{inv}}^2} \right] \quad (9)$$

272 where  $R_{\text{inv}}$  is the size of the source.

273 Assuming unpolarized emission, using the appropriately symmetrized form of  $\Psi$  (Eq. 7) with a spheri-  
 274 cally symmetric Gaussian source (Eq. 9), with the Koonin-Pratt equation (Eq. 4), the correlation function  
 275 for uncharged particles is given by [5]

$$C(k^*) = 1 + C_{\text{QI}}(k^*) + C_{\text{FSI}}(k^*) \quad (10)$$

276  $C_{\text{QI}}$  describes plane-wave quantum interference:

$$C_{\text{QI}}(k^*) = \alpha \exp(-4k^{*2}R^2) \quad (11)$$

277 where  $\alpha = (-1)^{2j}/(2j+1)$  for identical particles with spin  $j$ , and  $\alpha = 0$  for non-identical particles.  $C_{\text{FSI}}$   
 278 describes the s-wave strong final state interaction between the particles:

$$C_{\text{FSI}}(k^*) = \sum_S \rho_S \left[ \frac{1}{2} \left| \frac{f^S(k^*)}{R_{\text{inv}}} \right|^2 \left( 1 - \frac{d_0^S}{2\sqrt{\pi}R_{\text{inv}}} \right) + \frac{2\Re f^S(k^*)}{\sqrt{\pi}R_{\text{inv}}} F_1(2k^* R_{\text{inv}}) - \frac{\Im f^S(k^*)}{R_{\text{inv}}} F_2(2k^* R_{\text{inv}}) \right] \quad (12)$$

279 where

$$F_1(z) = \int_0^z \frac{e^{x^2-z^2}}{z} dx; \quad F_2(z) = \frac{1-e^{-z^2}}{z} \quad (13)$$

280 The weight factor,  $\rho_S$  is the normalized emission probability for a state of total spin  $S$ ; in the assumed  
 281 case of unpolarized emission,  $\rho_S = (2S+1)/[(2j_1+1)(2j_2+1)]$ , where  $j_{1,2}$  are the spins of the particles  
 282 in the pair.

283 An additional parameter  $\lambda$  is typically included in the femtoscopic fit function to account for the purity of  
 284 the pair sample, as well as the presence of any uncorrelated pairs. In the case of no residual correlations  
 285 (to be discussed in Section 3.3), the fit function becomes:

$$C(k^*) = 1 + \lambda [C_{\text{QI}}(k^*) + C_{\text{FSI}}(k^*)] \quad (14)$$

286 The presented formalism simplifies for the ΛK system. The particles in the pairs are obviously non-  
 287 identical, therefore  $\alpha = 0$ , and we need not worry about the quantum statistical term,  $C_{\text{QI}}$ . Furthermore,  
 288 Λ is spin-0 and K are spin-1/2, so the ΛK system only has one possible total spin state  $S$ , and therefore  
 289  $C_{\text{FSI}}$  has only a single term. In the following, we drop the  $S$  superscript from all scattering parameters.

290 **3.3 Residual Correlations**

291 The purpose of this analysis is study the interaction and scale of the emitting source of the primary ΛK  
 292 pairs. In order to obtain correct results, it is desirable for our particle collections to consist of primary  
 293 particles. In practice, this is impossible to achieve; many of our particles are not primary, but origi-  
 294 nate as decay products from other resonances. Some of our Λ hyperons decay from  $\Sigma^0$ ,  $\Xi^0$ ,  $\Xi^-$  and  
 295  $\Sigma^{*(+,-,0)}(1385)$  parents, and some of our K mesons decay from  $K^{*(+,-,0)}(892)$  parents. In these decays,  
 296 the daughter carries away a momentum very similar to that of its parent. As a result, the correlations be-  
 297 tween the particles in the daughter pair will be sensitive to, and dependent upon, the interaction between  
 298 the parents. In effect, the correlation between the parents will be visible, although smeared out, in the  
 299 daughters' signal. We call this a residual correlation resulting from feed-down. Residual correlations  
 300 are important in an analysis when three criteria are met [16]: i) the parent correlation signal is large,  
 301 ii) a large fraction of pairs in the sample originate from the particular parent system, and iii) the decay  
 302 momenta are comparable to the expected correlation width in  $k^*$ .

303 As it is difficult for us to eliminate these residual correlations in our analyses, we must attempt to account  
 304 for them in our fit. The genuine ΛK correlation function may be combined with the contributions from  
 305 residual feed-down and misidentified particles to obtain the final, measured correlation function:

$$C_{\text{measured}}(k_{\Lambda K}^*) = 1 + \lambda'_{\Lambda K}[C_{\Lambda K}(k_{\Lambda K}^*) - 1] + \sum_{i,j} \lambda'_{ij}[C_{ij}(k_{\Lambda K}^*) - 1] \quad (15)$$

$$\begin{aligned} \lambda'_{ij} &= \lambda_{\text{Fit}} \lambda_{ij} \\ \sum_{i,j} \lambda'_{ij} &= \lambda_{\text{Fit}} \sum_{i,j} \lambda_{ij} = \lambda_{\text{Fit}} \end{aligned}$$

306 where the ΛK term represents the genuine ΛK correlation, and the  $i, j$  terms denote the contributions  
 307 from residual feed-down and possible impurities. More specifically,  $C_{ij}(k_{\Lambda K}^*)$  is the correlation function  
 308 between parents of particle species  $i$  and  $j$ , expressed in the basis of the relative momentum of the  
 309 observed daughter ΛK pairs. The  $\lambda$  parameters serve as weight dictating the strength of the parent  
 310 contribution to the daughter pair, and are normalized to unity. The individual  $\lambda_{ij}$  are fixed (and whose  
 311 values can be found in Table A.1), but the parameter  $\lambda_{\text{Fit}}$  is left free. The  $\lambda_{\text{Fit}}$  parameter serves as an  
 312 overall normalization shared by all contributors.

313 In order to obtain the parent correlation function expressed in the relative momentum of the daughter  
 314 pair, one must use a transform matrix. The transform matrix describes the decay kinematics of the parent  
 315 system into the daughter, and maps the  $k^*$  of the parent pair onto that of the daughter. Using this matrix,  
 316 the transformed residual correlation function can be obtained:

$$C_{ij}(k_{\Lambda K}^*) \equiv \frac{\sum_{k_{ij}^*} C_{ij}(k_{ij}^*) T(k_{ij}^*, k_{\Lambda K}^*)}{\sum_{k_{ij}^*} T(k_{ij}^*, k_{\Lambda K}^*)} \quad (16)$$

317 The transform matrix is generated with the THERMINATOR 2 [17] simulation. It is formed for a given  
 318 parent pair,  $ij$ , by taking all ΛK pairs originating from  $ij$ , calculating the relative momentum of the

parents ( $k_{ij}^*$ ) and daughters ( $k_{\Lambda K}^*$ ), and filling a two-dimensional histogram with the values. The transform matrix is essentially an unnormalized probability distribution mapping the  $k^*$  of the parent pair to that of the daughter pair when one or both parents decay.

Femtoscopic analyses are sensitive to the pair emission structure at kinetic freeze-out. Therefore, in the eyes of femtoscopy, any particle born from a resonance decay before last rescattering is seen as primary. For our study, when including three residual contributors, we consider a particle to be primary if its parent has a proper decay length of  $c\tau < 10$  fm. When including ten residual contributors, we must reduce this number to  $c\tau < 4$  fm for consistency. Moving to ten contributors, we introduce feed-down from  $\Sigma^*$  and  $K^*$  resonances, with proper decay lengths of  $c\tau \approx 5$  fm and  $c\tau \approx 4$  fm, respectively. As these are considered non-primary for the case of ten contributors, so must any resonance with  $c\tau > 4$  fm.

As previously stated, the  $\lambda$  parameters dictate the strength of the parent contribution to the daughter pair. Therefore, the  $\lambda$  parameter for parent system AB can be estimated as the total number of ΛK pairs in our experimental sample originating from AB ( $N_{AB}$ ) divided by the total number of ΛK pairs ( $N_{Total}$ ):

$$\lambda_{AB} = \frac{N_{AB}}{N_{Total}} \quad (17)$$

The particle yields can be estimated using THERMINATOR 2 simulation ( $N_{ij}^{THERM}$ ), while the reconstruction efficiencies ( $RE_{ij}$ ) are estimated with MC HIJING data, which has been run through GEANT to simulate the detector response. Thus, the  $\lambda$  parameters are estimated as:

$$\lambda_{AB} = \frac{N_{AB}}{N_{Total}} = \frac{N_{AB}^{THERM} RE_{AB}^{HIJING}}{\sum_{ij} N_{ij}^{THERM} RE_{ij}^{HIJING}} \quad (18)$$

The  $\lambda$  values used can be found in Table A.1, for the case of both three and ten residual contributors. In the table, we also list the  $\lambda$  values used for “Other” and “Fakes”. The “Other” category contains pairs which are not primary, and which do not originate from the (3 or 10) residual pairs included in the fit. The “Fakes” category represents pairs that are mistakenly identified as ΛK. To estimate this  $\lambda_{Fakes}$  value, we assumed that the number of fake pairs was equal to the total number of pairs multiplied by the Λ purity (i.e. assuming perfect purity for the kaons); or, more simply,  $\lambda_{Fakes} = 1.0 - \text{Purity}(\Lambda)$ . For both of these contributors (“Other” and “Fakes”), we assume that these correlations average to unity, and therefore do not contribute to the final correlation function.

In practice, we model the correlation function of the parents (ex.  $\Sigma^0 K^+$ ), and run the correlation function through the appropriate transform matrix to determine the contribution to the daughter correlation function (ex.  $\Lambda K^+$ ). In an ideal world, we would simply look up the parent interaction in some table, and input this into our model, and form the parent correlation function,  $C_{ij}$ . Unfortunately, the world in which we live is not perfect, such a table does not exist, and little is known about the interaction between the particles in the residual pairs of this study. Additionally, introducing a unique set of scattering parameters and radii for each residual system would introduce a large number of additional fit parameters, for which we do not have many constraints, and would cause our fitter to be too unconstrained and yield untrustworthy results. For this analysis, we assume all residual pairs have the same source size as the daughter pair. Furthermore, we assume Coulomb-neutral residual pairs share the same scattering parameters as the daughter pair. Therefore, for Coulomb-neutral pairs, such as  $\Sigma^0 K$ , and  $\Xi^0 K$ ,  $C_{ij}(k_{ij}^*)$  is calculated from Eqn. 10, with the help of Eqn. 12;  $C_{ij}(k_{\Lambda K}^*)$  is then obtained by transforming  $C_{ij}(k_{ij}^*)$  with Eq. 16, using the appropriate transform matrix.

For residual pairs affected by both the strong and Coulomb interactions, things are a bit more complicated. This is due to the fact that, for the case of both strong and Coulomb interaction, we no longer have a nice analytical form with which to fit. Generating a correlation function including both is also

time consuming, as described further in Appendix C. When modeling  $\Xi^- K^\pm$  residual correlations, we use the experimental  $\Xi^- K^\pm$  data; in this case, there is no need to make any assumptions about scattering parameters or source sizes. For the other cases, we assume the strong interaction is negligible, and generate the parent correlation assuming a Coulomb-only scenario (see Appendix C for more details). This approximation is well justified here as a Coulomb-only description of the system describes, reasonably well, the broad features of the correlation; the strong interaction is necessary for the fine details. However, as these correlations are run through a transform matrix, which largely flattens out and fine details, a Coulomb-only description should be sufficient. This is reinforced by the fact that we find consistent results between using the  $\Xi K$  data and the Coulomb-only model of the  $\Xi K$  data in our treatment of the residual contribution.

### 369 3.4 Momentum Resolution Corrections

Finite track momentum resolution causes the reconstructed momentum of a particle to smear around the true value. This, of course, also holds true for V0 particles. The effect is propagated up to the pairs of interest, which causes the reconstructed relative momentum ( $k_{\text{Rec}}^*$ ) to differ from the true momentum ( $k_{\text{True}}^*$ ). Smearing of the momentum typically will result in a suppression and broadening of the signal.

The effects of finite momentum resolution can be investigated using the MC data, for which both the true and reconstructed momenta are available. Information gained from looking at  $k_{\text{Rec}}^*$  vs  $k_{\text{True}}^*$  can be exploited to generate response matrices. A response matrix describes quantitatively how each  $k_{\text{Rec}}^*$  bin receives contributions from multiple  $k_{\text{True}}^*$  bins, and can be used to account for the effects of finite momentum resolution. With this approach, the resolution correction is applied on-the-fly during the fitting process by propagating the theoretical (fit) correlation function through the response matrix, according to:

$$C_{\text{fit}}(k_{\text{Rec}}^*) = \frac{\sum_{k_{\text{True}}^*} M_{k_{\text{Rec}}^*, k_{\text{True}}^*} C_{\text{fit}}(k_{\text{True}}^*)}{\sum_{k_{\text{True}}^*} M_{k_{\text{Rec}}^*, k_{\text{True}}^*}} \quad (19)$$

where  $M_{k_{\text{Rec}}^*, k_{\text{True}}^*}$  is the response matrix,  $C_{\text{fit}}(k_{\text{True}}^*)$  is the fit binned in  $k_{\text{True}}^*$ , and the denominator normalizes the result. Equation 19 describes that, for a given  $k_{\text{Rec}}^*$  bin, the observed value of  $C(k_{\text{Rec}}^*)$  is a weighted average of all  $C(k_{\text{True}}^*)$  values, where the weights are the normalized number of counts in the  $[k_{\text{Rec}}^*, k_{\text{True}}^*]$  bin.

### 385 3.5 Non-Flat Background

We observe a significant non-femtoscopic, non-flat, background in all of our correlations at large  $k^*$ . This background increases with decreasing centrality, is the same amongst all  $\Lambda K^\pm$  pairs, and is more pronounced in the  $\Lambda K_S^0$  system. This difference in  $\Lambda K^\pm$  and  $\Lambda K_S^0$  backgrounds is due mainly to the difference in kinematic cuts, not due to any interesting physics.

It is suggested that this background effect is due primarily to particle collimation associated with elliptic flow [18]. More specifically, these backgrounds result from mixing events with unlike event-plane angles ( $\Psi_{\text{EP}}$ ). As explained in [18], when elliptic flow is present, all particles are more likely to be emitted in a specific direction (in-plane), as opposed to a perpendicular direction. Therefore, the difference in momenta for pairs of particles tends to be smaller, compared to the case of no flow. In the case of mixed-event pairs, the two events used do not share an event-plane, and therefore there is no collimation effect in the pairs from flow. As a result, pairs with larger momentum are more likely when mixed-events are used (in the denominator of the correlation function), causing the correlation function to dip below unity. This same reasoning suggests that the background should lead to an enhancement at low- $k^*$ .

399 The issue here is that we need to know the behavior of the non-femtoscopic background in the low-  
 400  $k^*$  region, but we only cleanly observe it in the region further out where there is no femtoscopic signal.  
 401 Unfortunately, we cannot simply rotate each event to artificially align their event-planes and rid ourselves  
 402 of this mixing effect, as our azimuthal angle acceptance is not perfectly uniform, and we have only finite  
 403 event-plane resolution. With better resolution, one could simply bin events in  $\Psi_{EP}$  and only mix events  
 404 within a given bin. We pursued this direction, and observed a slight decrease in the background; however,  
 405 going to finer binning, we saw no additional reduction in the background, signaling that we had reached  
 406 the limits dictated by the resolution. In the end, we are forced to model the background to include it into  
 407 our fit.

408 THERMINATOR 2 simulation has been shown to reproduce the background features in a  $\pi K$  analysis  
 409 [18]. After issuing each simulated event a random  $\Psi_{EP}$ , we found THERMINATOR 2 did an exceptional  
 410 job of describing our data. Furthermore, the simulation showed the non-femtoscopic background affects  
 411 the correlation function as a separable scale factor. Figure 4 shows the THERMINATOR 2 simulation  
 412 (gold) together with experimental data (red, blue, or black). The figure also shows a 6<sup>th</sup>-order polynomial  
 413 fit to the simulation (gold), as well as the fit polynomial scaled to match the data (red, blue, black).

414 The description by THERMINATOR 2 of the non-femtoscopic backgrounds in the  $\Lambda K^\pm$  systems is re-  
 415 markable, and can be used in a quantitative fashion to help fit the data. More specifically, the non-  
 416 femtoscopic backgrounds were modeled by (6<sup>th</sup>-)order polynomial fits to THERMINATOR 2 simulation  
 417 for the  $\Lambda K^\pm$  analyses; one polynomial for each centrality class. The form of each polynomial was set  
 418 before use with the experimental data, by fitting to the THERMINATOR 2 simulation, shown in Fig. 4.  
 419 At the time of the fit, the polynomial used to correct each correlation function could only be adjust by a  
 420 simple scale factor to best match the data.

421 The description of the  $\Lambda K_S^0$  is good at a qualitative level, but not quantitatively good enough to be utilized  
 422 in our fit. As such, we use a linear form to model the background in the  $\Lambda K_S^0$  system. The background for  
 423 each correlation function was fixed before use in the signal region by fitting a linear form to the region  
 424  $0.6 < k^* < 0.9$  GeV/c. In all cases, the non-femtoscopic background correction was applied as a scale  
 425 factor.

426 An alternative approach to treating the non-femtoscopic background is to instead attempt to eliminate  
 427 it. The background may be effectively reduced by forming the reference distribution ( $B(k^*)$ ) with the  
 428 “Stavinskiy method”. With the Stavinskiy method, mixed-event pairs are not used for the reference  
 429 distribution; instead, same-event pseudo-pairs, formed by rotating one particle in a real pair by 180°  
 430 in the transverse plane, are used. This rotation rids the pairs of any femtoscopic correlation, while  
 431 maintaining correlations due to elliptic flow (and other suitably symmetric contributors). The effect on  
 432 our  $\Lambda K^+$  correlation functions can be seen in the appendix, in Fig. B.1.

### 433 3.6 Summarized Fit Procedure

434 A simple  $\chi^2$  test is inappropriate for fitting correlation functions, as the ratio two Poisson distributions  
 435 does not result in a Poisson distribution. Instead, a log-likelihood fit function of the following form is  
 436 used [1]:

$$\chi_{PML}^2 = -2 \left[ A \ln \left( \frac{C(A+B)}{A(C+1)} \right) + B \ln \left( \frac{A+B}{B(C+1)} \right) \right] \quad (20)$$

437 where  $A$  is the experimental signal distribution (numerator),  $B$  is the experimental reference distribution  
 438 (denominator), and  $C$  is the theoretical fit correlation function. Therefore, we use Eq. 20 as the statistic  
 439 quantifying the quality of the fit. The parameters of the fit are:  $\lambda$ ,  $R$ ,  $f_0$  ( $\Re f_0$  and  $\Im f_0$  separately),  $d_0$ ,  
 440 and normalization  $N$ .

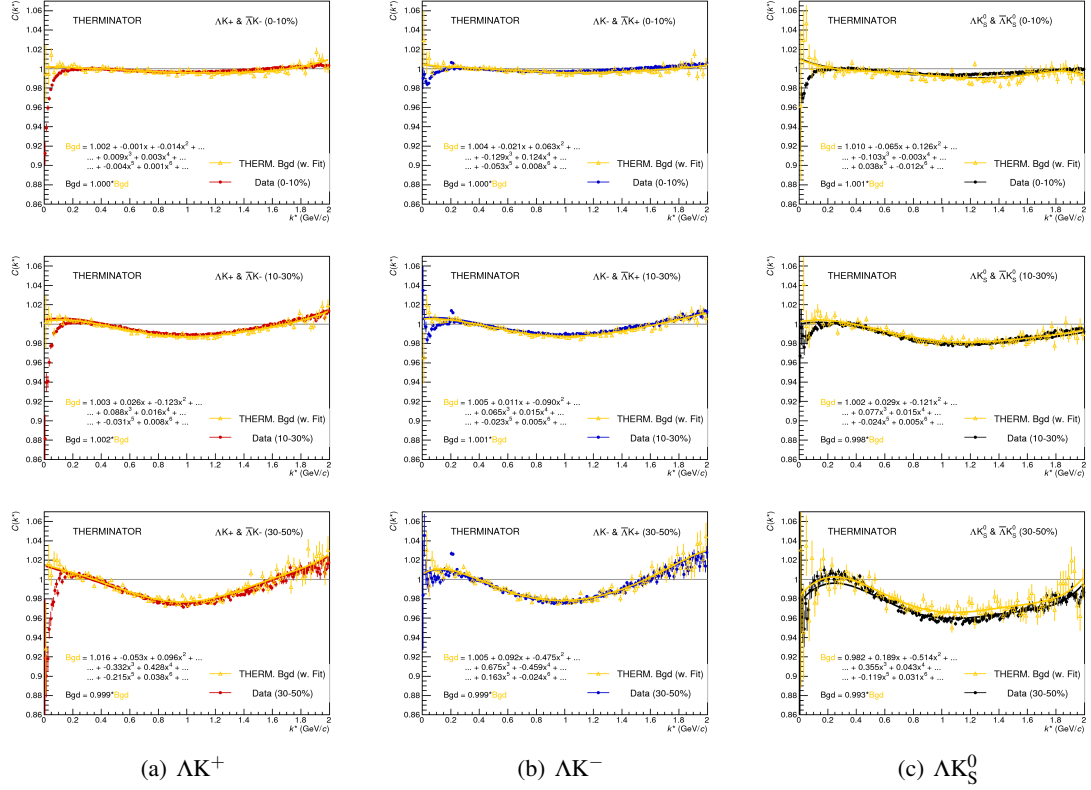


**Fig. 4:** THERMINATOR 2 simulation (gold) together with experimental data (red, blue, or black). The left column shows results for  $\Lambda K^+$  (4(a)), middle for  $\Lambda K^-$  (4(b)), and right for  $\Lambda K_S^0$  (4(c)). A 6<sup>th</sup>-order polynomial fit to the simulation is shown as a solid gold line, and whose fit parameters are printed on the lower left of each plot. This polynomial is scaled to match the experimental data; the value of this scale is printed in the lower left corner of each plot. The polynomial fit with scale factor applied is drawn in a color matching the experimental data (red, blue, black).

- 441 With our procedure, we are able to share parameters between different analyses and fit all simultaneously.  
 442 A given pair and its conjugate (e.g.  $\Lambda K^+$  and  $\bar{\Lambda} K^-$ ) always share scattering parameters ( $\Re f_0$ ,  $\Im f_0$ ,  $d_0$ ).  
 443 However, the three distinct analyses ( $\Lambda K^+$ ,  $\Lambda K^-$ , and  $\Lambda K_S^0$ ) are assumed to have scattering parameters  
 444 unique from each other. We assume the pair emission source for a given centrality class is similar between  
 445 all analyses; therefore, for each centrality, all  $\Lambda K$  analyses share a common radius parameter. We assume  
 446 the same is true for the overall normalization  $\lambda$  parameters in Eq. 16. Finally, each correlation function  
 447 has a unique normalization parameter.
- 448 All correlation functions were normalized in the range  $0.32 < k^* < 0.40$  GeV/c, and fit in the range  $0.0$   
 449  $< k^* < 0.30$  GeV/c. For the  $\Lambda K^-$  analysis, the region  $0.19 < k^* < 0.23$  GeV/c was excluded from the  
 450 fit to exclude the bump caused by the  $\Omega^-$  resonance. For each pair system, we account for contributions  
 451 from three residual contributors, as discussed in Sec. 3.3, and whose individual  $\lambda$  values are listed in  
 452 Table A.1 (the cases of zero and ten residual contributors were also investigated, but the case of three  
 453 contributors was deemed most reasonable). We account for effects of finite track momentum resolution,  
 454 as outlined in Sec. 3.4. The non-femtoscopic backgrounds are modeled using the THERMINATOR 2  
 455 simulation for the  $\Lambda K^\pm$  analyses, and with a linear form for the  $\Lambda K_S^0$  system, as described in Sec. 3.5. In  
 456 general, corrections are applied to the fit function, the raw data is never touched.
- 457 To summarize, the complete fit function is constructed as follows:

- 458 1. The uncorrected, primary, correlation function,  $C_{\Lambda K}(k_{\text{True}}^*)$ , is constructed using Eqns. 10 and 12

- 459    2. The correlation functions describing the parent systems which contribute residually are obtained  
460    using:
  - 461    – Eqns. 10 and 12 for the case of Coulomb-neutral pairs
  - 462    –  $\Xi^- K^\pm$  experimental data for  $\Xi^- K^\pm$  contributions
  - 463    – a Coulomb-only curve, with the help of Appendix C, for other pairs including the Coulomb  
464    interaction
- 465    3. The residual contributions to the  $\Lambda K$  correlation function is found by running each parent correla-  
466    tion function through the appropriate transform matrix, via Eq.16
- 467    4. The primary and residual correlations are combined, via Eq.15 with Tab. A.1, to form  $C'_{Fit}(k_{\text{True}}^*)$
- 468    5. The correlation function is corrected to account for momentum resolution effects using Eq. 19, to  
469    obtain  $C'_{Fit}(k_{\text{Rec}}^*)$
- 470    6. Finally, the non-flat background correction,  $F_{\text{Bgd}}(k_{\text{Rec}}^*)$  is applied, and the final fit function is ob-  
471    tained,  $C_{\text{Fit}}(k_{\text{Rec}}^*) = C'_{\text{Fit}}(k_{\text{Rec}}^*) * F_{\text{Bgd}}(k_{\text{Rec}}^*)$

### 472    3.7 Systematic uncertainties

473    In order to understand the systematic uncertainties of our data, the analysis code was run many times  
474    using slightly different values for a number of important cuts, and the results were compared. To quantify  
475    the systematic errors on the data, all correlation functions built using all varied cut values were bin-by-  
476    bin averaged, and the resulting variance of each bin was taken as the systematic error. The cuts included  
477    in the systematic study, as well as the values used in the variations, are shown in Tab. 4 ( $\Lambda K_S^0$ ) and Tab.  
478    5 ( $\Lambda K^\pm$ ). Note, the central value corresponds to that used in the analysis.

479    Similarly, the fit parameters extracted from all of these correlation functions were averaged, and the  
480    resulting variances were taken as the systematic errors for the fit parameters. As with the systematic  
481    errors on the data, this was performed for all varied cut values. Additionally, a systematic analysis  
482    was done on our fit method through varying our  $k^*$  fit range, as well as varying our modeling of the  
483    non-femtoscopic background. Our choice of  $k^*$  fit range was varied by  $\pm 25\%$ . As previously stated,  
484    the non-femtoscopic backgrounds are modeled using the THERMINATOR 2 simulation for the  $\Lambda K^\pm$   
485    analyses, and with a linear form for the  $\Lambda K_S^0$  system. To study the contribution of this choice to our  
486    systematic errors, we modeled the backgrounds of all of our systems by fitting to the data with a with a  
487    linear, quadratic, and Gaussian form. Additionally, we modeled the backgrounds of all systems with a  
488    polynomial fit to the THERMINATOR simulation, scaled to match the data. The resulting uncertainties  
489    in the extracted parameter sets were combined with our uncertainties arising from our particle and pair  
490    cuts.

## 491    4 Results

492    Figure 5 shows our  $\Lambda K$  data with fits for all studied centrality bins (0-10%, 10-30%, and 30-50%). All  
493    analyses were fit simultaneously across all centralities, with a single radius and normalization  $\lambda$  param-  
494    eter for each centrality bin. Scattering parameters ( $\Re f_0$ ,  $\Im f_0$ ,  $d_0$ ) were shared between pair-conjugate  
495    systems, but assumed unique between the different  $\Lambda K$  charge combinations (i.e. a parameter set de-  
496    scribing the  $\Lambda K^+$  &  $\bar{\Lambda} K^-$  system, a second set describing the  $\Lambda K^-$  &  $\bar{\Lambda} K^+$  system, and a third for the  
497     $\Lambda K_S^0$  &  $\bar{\Lambda} K_S^0$  system). Each correlation function received a unique normalization parameter. The fits  
498    were corrected for finite momentum resolution effects, non-femtoscopic backgrounds, and residual cor-  
499    relations resulting from the feed-down from resonances. In Fig. 5, lines represent statistical errors, while  
500    boxes represent systematic errors. The black solid curve shows the primary ( $\Lambda K$ ) contribution to the fit,

$\Lambda K_S^0$  systematics

$\Lambda K_S^0$ systematics	
DCA $\Lambda(\bar{\Lambda})$	4, 5, 6 mm
DCA $K_S^0$	2, 3, 4 mm
DCA $\Lambda(\bar{\Lambda})$ Daughters	3, 4, 5 mm
DCA $K_S^0$ Daughters	2, 3, 4 mm
$\Lambda(\bar{\Lambda})$ Cosine of Pointing Angle	0.9992, 0.9993, 0.9994
$K_S^0$ Cosine of Pointing Angle	0.9992, 0.9993, 0.9994
DCA to Primary Vertex of $p(\bar{p})$ Daughter of $\Lambda(\bar{\Lambda})$	0.5, 1, 2 mm
DCA to Primary Vertex of $\pi^-(\pi^+)$ Daughter of $\Lambda(\bar{\Lambda})$	2, 3, 4 mm
DCA to Primary Vertex of $\pi^+$ Daughter of $K_S^0$	2, 3, 4 mm
DCA to Primary Vertex of $\pi^-$ Daughter of $K_S^0$	2, 3, 4 mm
Average Separation of Like-Charge Daughters	5, 6, 7 cm

**Table 4:**  $\Lambda K_S^0$  systematics $\Lambda K^\pm$  systematics

$\Lambda K^\pm$ systematics	
DCA $\Lambda(\bar{\Lambda})$	4, 5, 6 mm
DCA $\Lambda(\bar{\Lambda})$ Daughters	3, 4, 5 mm
$\Lambda(\bar{\Lambda})$ Cosine of Pointing Angle	0.9992, 0.9993, 0.9994
DCA to Primary Vertex of $p(\bar{p})$ Daughter of $\Lambda(\bar{\Lambda})$	0.5, 1, 2 mm
DCA to Primary Vertex of $\pi^-(\pi^+)$ Daughter of $\Lambda(\bar{\Lambda})$	2, 3, 4 mm
Average Separation of $\Lambda(\bar{\Lambda})$ Daughter with Same Charge as $K^\pm$	7, 8, 9 cm
Max. DCA to Primary Vertex in Transverse Plane of $K^\pm$	1.92, 2.4, 2.88
Max. DCA to Primary Vertex in Longitudinal Direction of $K^\pm$	2.4, 3.0, 3.6

**Table 5:**  $\Lambda K^\pm$  systematics

501 the green curve shows the fit to the non-femtoscopic background, and the purple curve shows the final  
 502 fit after all corrections have been applied. The extracted fit values with uncertainties are printed as (fit  
 503 value)  $\pm$  (statistical uncertainty)  $\pm$  (systematic uncertainty).

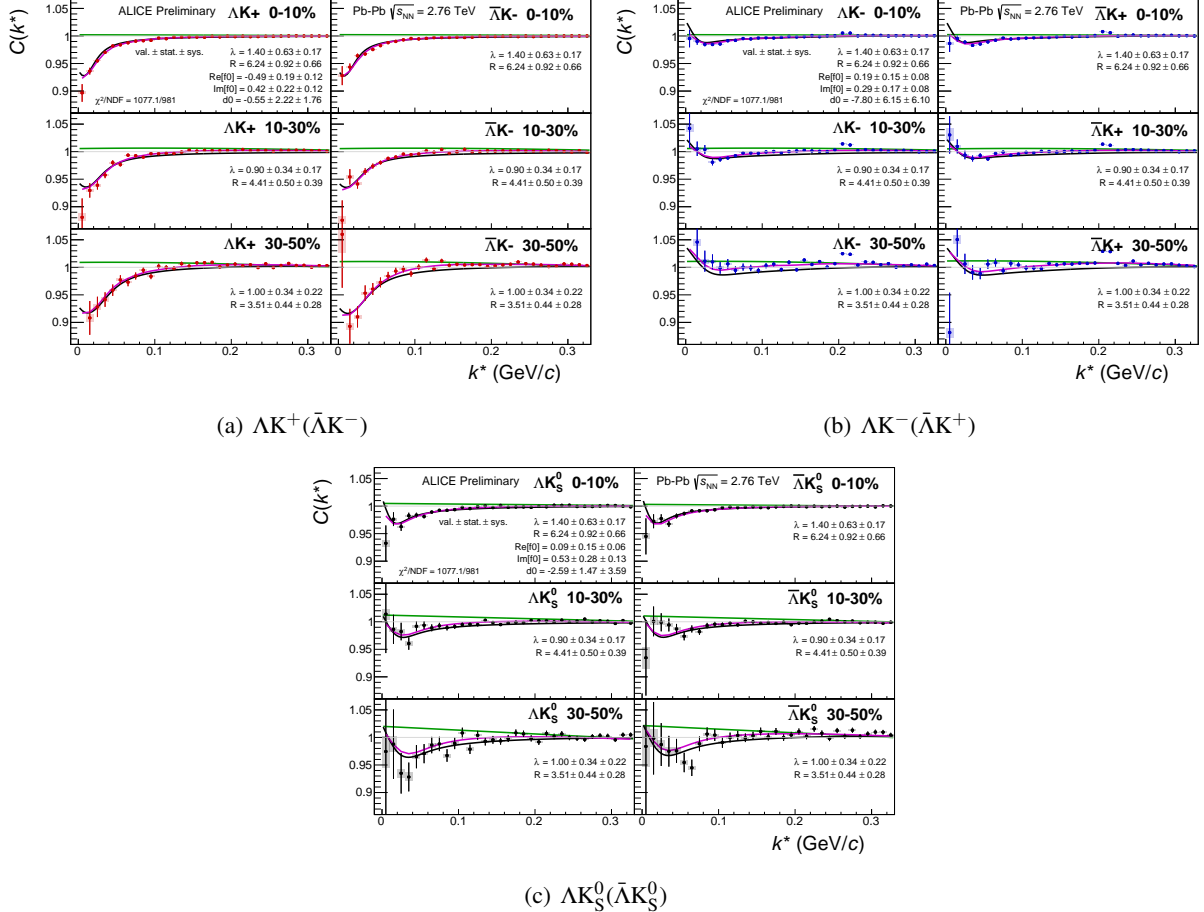


**Fig. 5:** Fits, with 3 residual correlations included, for all ΛK analyses across all studied centralities (0-10%, 10-30%, and 30-50%). The lines represent the statistical errors, while the boxes represent the systematic errors. The black solid line represents the primary ( $\Lambda K$ ) correlation's contribution to the fit. The green line shows the fit to the non-flat background. The purple points show the fit after all residuals' contributions have been included, and momentum resolution and non-flat background corrections have been applied. The extracted fit values with uncertainties are printed.

504 Figure 6 summarizes well our results. In the summary plot, we show the extracted scattering parameters  
 505 in the form of a  $\Im(f_0)$  vs  $\Re(f_0)$  plot, which includes the  $d_0$  values to the right side. We also show the  $\lambda$   
 506 vs. radius parameters for all three of our studied centrality bins. In addition to our results, we show  
 507 theoretical predictions made using chiral perturbation theory [19, 20].

508 We extract positive imaginary parts,  $\Im(f_0)$ , of the scattering lengths for all systems. We expect this,  
 509 as  $\Im(f_0)$  describes the inelastic scattering channels. More interestingly, our results show that the  $\Lambda K^+$   
 510 and  $\Lambda K^-$  systems differ in the sign of the real part,  $\Re(f_0)$ , of their scattering lengths (negative for  
 511  $\Lambda K^+$ , and positive for  $\Lambda K^-$ ). Furthermore, each of the three systems has a  $\Re(f_0)$  unique from the  
 512 others. The real part of the scattering length describes the effect of the strong interaction, making the  
 513 difference in these systems quite intriguing. A positive  $\Re(f_0)$  signifies that the effect of the strong force  
 514 is attractive, while a negative  $\Re(f_0)$  signifies a repulsion. We suggest that this difference could be due to  
 515 an effect arising from different quark-antiquark interactions between the pairs ( $s\bar{s}$  in  $\Lambda K^+$ ,  $u\bar{u}$  in  $\Lambda K^-$ ).  
 516 An alternative explanation could be that the effect is due to the different net strangeness for each system.

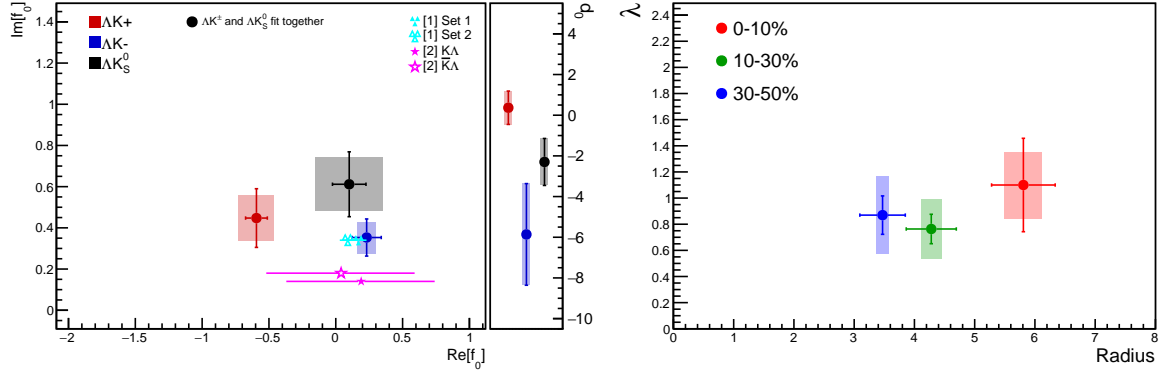


**Fig. 6:** Extracted scattering parameters for all of our ΛK systems. [Left]:  $\Im(f_0)$  vs.  $\Re(f_0)$ , together with  $d_0$  to the right. [Right]:  $\lambda$  vs. Radius for the studied centrality bins (0-10%, 10-30%, 30-50%). The green [19] and yellow [20] points show theoretical predictions made using chiral perturbation theory.

517 More specifically, systems with less net strangeness have more channels into which they can decay,  
 518 causing a scarcity of pairs, i.e. a greater suppression of the correlation function, at low- $k^*$ . However, an  
 519 effect such as this really should instead manifest itself in  $\Im(f_0)$  not  $\Re(f_0)$ . In any case, this remains a  
 520 very interesting effect which needs an explanation.

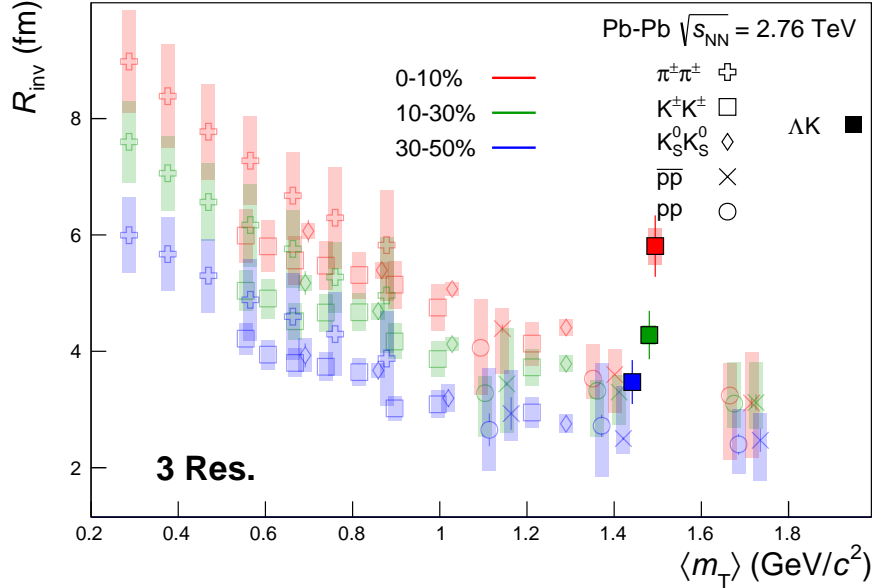


**Fig. 7:** 3 residual correlations in AK fits. Extracted fit  $R_{\text{inv}}$  parameters as a function of pair transverse mass ( $m_T$ ) for various pair systems over several centralities. The ALICE published data [2] is shown with transparent, open symbols.

521 A comparison of our extracted radii to those of other systems measured by ALICE [2] is shown in Figure  
 522 7. The figure shows extracted  $R_{\text{inv}}$  vs.  $m_T$  for several centralities and for several different systems. The  
 523 radii are observed to increase for more central events, as expected from a simple geometric picture of the  
 524 collisions. They also demonstrate a decreasing size with increasing  $m_T$ , as expected in the presence of  
 525 collective radial flow [3]. It was found that [4], even in the presence of good global  $m_T$ -scaling for the  
 526 three-dimensional radii in the LCMS frame, a particle species dependence will exist for the  $R_{\text{inv}}$  measured  
 527 in the PRF, due to trivial kinematic reasons. These kinematic effects, resulting from the transformation  
 528 from LCMS to PRF, causes smaller masses to exhibit larger  $R_{\text{inv}}$  [2] (explaining, for instance, how the  
 529 pion radii are systematically higher than kaon radii at the same approximate  $m_T$ ).

It is clear from the results that the ΛK systems do not conform to the approximate  $m_T$ -scaling of the pair source sizes.<sup>1</sup> At first thought, this may appear to be a troubling result; the approximate scaling is an observed consequence of the collective behavior of the soft (low- $p_T$ ) sector of the produced system. The Λ and K particles certainly participate in the collective expansion of the QGP medium, but, importantly, they are non-identical particles. Taking a closer look at Fig. 7, one can see that the previously published data (transparent points), and the established (approximate)  $m_T$ -scaling trend, are for identical particle analyses only. When dealing with non-identical particles, the pair emission source, which is measured by femtoscopy, is the superposition of two single-particle sources. In general, each single-particle source will have its own size, shape, and space-time position within the produced medium, which is unique from its paired partner. The hydrodynamic nature of the medium produces the approximate  $m_T$ -scaling with respect to these single-particle sources, not the pair sources. The combination of two unique sources separated in space-time, when probing correlations between non-identical particle pairs, leads to extracted radii falling outside of the (identical particle femtoscopy)  $m_T$ -scaling trend.

It is well established that non-identical particle femtoscopic studies are able to probe deeper than the second moments of the pair distribution functions accessed via identical particle studies. In addition to this, non-identical particle studies are able to measure the relative emission shifts, the first moments of the emission function. For the study of ΛK pairs at mid-rapidity in Pb-Pb collisions, we expect a separation of the single-particle sources in the out direction. One elegant method for extracting information about the emission asymmetries is via a spherical decomposition of the correlation function. With this method, one can draw a wealth of information from just a few components of the decomposition. Particularly, the  $C_{00}$  component is similar to the 1D correlation functions typically studied, and probes the overall size of the source. The  $\Re C_{11}$  component probes the asymmetry of the system in the out direction; a non-zero value reveals the asymmetry. Figure D.1 in App. D shows the  $C_{00}$  and  $\Re C_{11}$  components of the spherical decomposition of our  $\Lambda K^+$  data in the 0-10% centrality bin. The  $\Re C_{11}$  component shows a clear deviation from zero, and the negative value signifies that the Λ particles are, on average, emitted further out and/or earlier than the K mesons. This effect is supported by the results obtained from the THERMINATOR 2 model, shown in Fig. E.1. The effect of a non-zero shift in the source will naturally lead to larger measured radii. This is intuitive, and also reaffirmed in our simulation with THERMINATOR 2 shown in App. E. We have also shown larger effective radii to result from inserting a Gaussian source with a non-zero shift into the Koonin-Pratt equation and numerically integrating.

## 5 Summary

Results from a femtoscopic analysis of ΛK correlations in Pb-Pb collisions at  $\sqrt{s_{NN}} = 2.76$  TeV with ALICE at the LHC have been presented. The femtoscopic radii,  $\lambda$  parameters, and scattering parameters were extracted from one-dimensional correlation functions in terms of the invariant momentum difference. The scattering parameters of ΛK pairs in all three charge combinations ( $\Lambda K^+$ ,  $\Lambda K^-$ , and  $\Lambda K_S^0$ ) have been measured for the first time. We observe a striking difference in the  $\Lambda K^+$  and  $\Lambda K^-$  correlation functions, which is reflected in the unique set of scattering parameters extracted for each. The  $\Lambda K^+$  systems exhibits a negative  $\Re(f_0)$ , while that extracted from the  $\Lambda K^-$  system is positive. The physics underlying this phenomenon is currently not well understood, but we suggest this could be due

<sup>1</sup> For our non-identical particle pairs, to be more directly analogous to the single particle  $m_T$ , we define the pair transverse mass as

$$\begin{aligned} m_{T,\text{pair}}^2 &= \left(\frac{m_{\text{inv}}}{2}\right)^2 + \left(\frac{1}{2}|p_{T,1} + p_{T,2}|\right)^2 \\ &= (K^0)^2 - (K^3)^2 \\ \text{where } K^\mu &\equiv \frac{1}{2}(p_1^\mu + p_2^\mu) \end{aligned}$$

569 to different quark-antiquark interactions between the pairs, or from different net strangeness for each  
 570 system. Finally, we find that the  $\Lambda$ K systems exhibit source radii larger than expected from extrapolation  
 571 from identical particle femtoscopic studies. We understand this effect to result from the separation in  
 572 space-time of the single-particle  $\Lambda$  and K source distributions.

## 573 Acknowledgements

## 574 References

- 575 [1] M. A. Lisa, S. Pratt, R. Soltz, and U. Wiedemann, “Femtoscopy in relativistic heavy ion  
 576 collisions,” *Ann. Rev. Nucl. Part. Sci.* **55** (2005) 357–402, arXiv:nucl-ex/0505014  
 577 [nucl-ex].
- 578 [2] ALICE Collaboration, J. Adam *et al.*, “One-dimensional pion, kaon, and proton femtoscopy in  
 579 Pb-Pb collisions at  $\sqrt{s_{NN}} = 2.76$  TeV,” *Phys. Rev.* **C92** no. 5, (2015) 054908, arXiv:1506.07884  
 580 [nucl-ex].
- 581 [3] S. V. Akkelin and Yu. M. Sinyukov, “The HBT interferometry of expanding sources,” *Phys. Lett.*  
 582 **B356** (1995) 525–530.
- 583 [4] A. Kisiel, M. Gaayn, and P. Boek, “Pion, kaon, and proton femtoscopy in Pb-Pb collisions at  
 584  $\sqrt{s_{NN}} = 2.76$  TeV modeled in (3+1)D hydrodynamics,” *Phys. Rev.* **C90** no. 6, (2014) 064914,  
 585 arXiv:1409.4571 [nucl-th].
- 586 [5] R. Lednický and V. L. Lyuboshitz *Sov. J. Nucl. Phys.* **35** (1982) 770.
- 587 [6] ALICE Collaboration, K. Aamodt *et al.*, “The alice experiment at the cern lhc,” *JINST* **3** (2008)  
 588 S08002. <http://stacks.iop.org/1748-0221/3/i=08/a=S08002>.
- 589 [7] ALICE Collaboration, B. Abelev *et al.*, “Centrality determination of Pb-Pb collisions at  $\sqrt{s_{NN}} =$   
 590 2.76 TeV with ALICE,” *Phys. Rev.* **C88** no. 4, (2013) 044909, arXiv:1301.4361 [nucl-ex].
- 591 [8] J. Alme *et al.*, “The ALICE TPC, a large 3-dimensional tracking device with fast readout for  
 592 ultra-high multiplicity events,” *Nucl. Instrum. Meth. A* **622** (2010) 316–367, arXiv:1001.1950  
 593 [physics.ins-det].
- 594 [9] ALICE Collaboration, B. B. Abelev *et al.*, “Performance of the ALICE Experiment at the CERN  
 595 LHC,” *Int. J. Mod. Phys.* **A29** (2014) 1430044, arXiv:1402.4476 [nucl-ex].
- 596 [10] A. Akindinov *et al.*, “Performance of the ALICE Time-Of-Flight detector at the LHC,” *Eur. Phys.*  
 597 *J. Plus* **128** (2013) 44.
- 598 [11] X.-N. Wang and M. Gyulassy, “hijing: A Monte Carlo model for multiple jet production in pp,  
 599 pA, and AA collisions,” *Phys. Rev. D* **44** (Dec, 1991) 3501–3516.  
 600 <https://link.aps.org/doi/10.1103/PhysRevD.44.3501>.
- 601 [12] R. Brun, F. Bruyant, F. Carminati, S. Giani, M. Maire, A. McPherson, G. Patrick, and L. Urban,  
 602 “GEANT Detector Description and Simulation Tool.”
- 603 [13] Particle Data Group Collaboration, C. Patrignani *et al.*, “Review of Particle Physics,” *Chin.*  
 604 *Phys.* **C40** no. 10, (2016) 100001.
- 605 [14] S. E. Koonin, “Proton Pictures of High-Energy Nuclear Collisions,” *Phys. Lett.* **B70** (1977) 43–47.
- 606 [15] S. Pratt, T. Csorgo, and J. Zimanyi, “Detailed predictions for two pion correlations in  
 607 ultrarelativistic heavy ion collisions,” *Phys. Rev.* **C42** (1990) 2646–2652.

- 608 [16] A. Kisiel, H. Zbroszczyk, and M. Szymaski, “Extracting baryon-antibaryon strong interaction  
609 potentials from p $\bar{\Lambda}$  femtoscopic correlation functions,” *Phys. Rev.* **C89** no. 5, (2014) 054916,  
610 arXiv:1403.0433 [nucl-th].
- 611 [17] M. Chojnacki, A. Kisiel, W. Florkowski, and W. Broniowski, “THERMINATOR 2: THERMal  
612 heavy IoN generATOR 2,” *Comput. Phys. Commun.* **183** (2012) 746–773, arXiv:1102.0273  
613 [nucl-th].
- 614 [18] A. Kisiel, “Non-identical particle correlation analysis in the presence of non-femtoscopic  
615 correlations,” *Acta Physica Polonica B* **48** (04, 2017) 717.
- 616 [19] Y.-R. Liu and S.-L. Zhu, “Meson-baryon scattering lengths in HB chi PT,” *Phys. Rev.* **D75** (2007)  
617 034003, arXiv:hep-ph/0607100 [hep-ph].
- 618 [20] M. Mai, P. C. Bruns, B. Kubis, and U.-G. Meissner, “Aspects of meson-baryon scattering in three  
619 and two-flavor chiral perturbation theory,” *Phys. Rev.* **D80** (2009) 094006, arXiv:0905.2810  
620 [hep-ph].
- 621 [21] A. Stavinskiy *et al.*, “Some new aspects of femtoscopy at high energy,” *Nukleonika* **49**  
622 (**Supplement 2**) (2004) S23.
- 623 [22] R. Lednický, “Finite-size effects on two-particle production in continuous and discrete spectrum,”  
624 *Phys. Part. Nucl.* **40** (2009) 307–352, arXiv:nucl-th/0501065 [nucl-th].

625 A  $\lambda$  Parameters

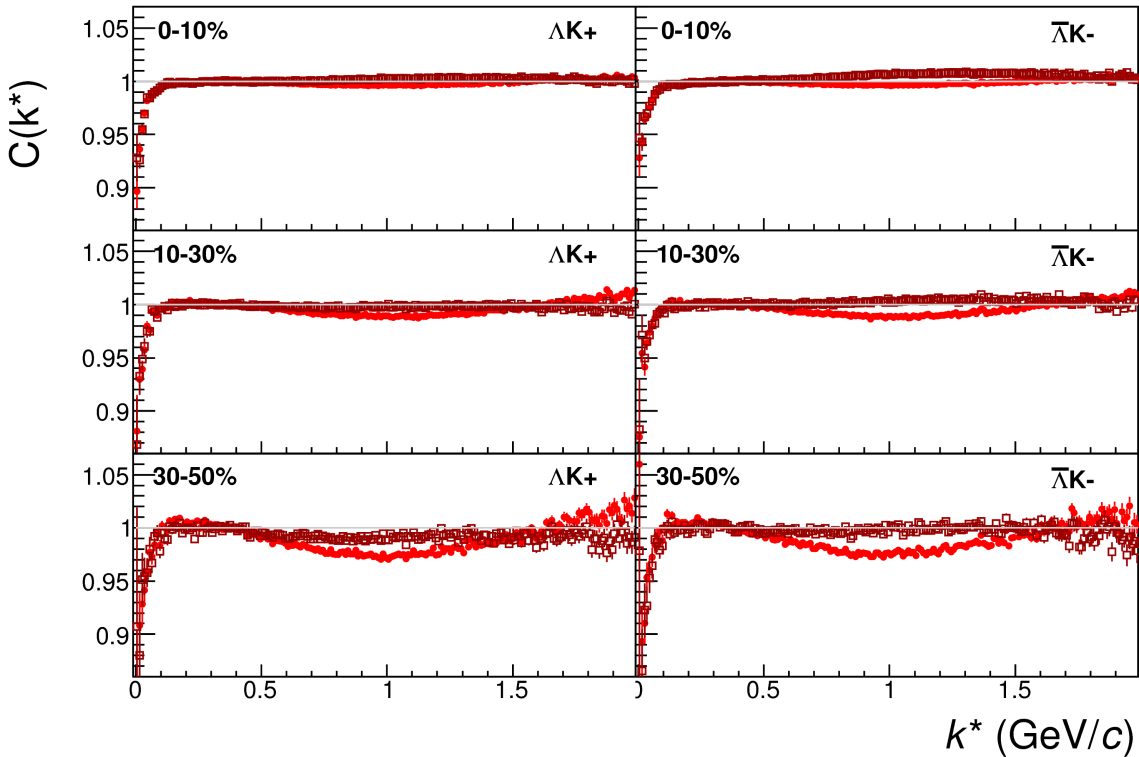
AK <sup>+</sup> residuals		$\bar{\Lambda}K^-$ residuals		AK <sup>-</sup> residuals		$\bar{\Lambda}K^+$ residuals		AK <sub>S</sub> <sup>0</sup> residuals		$\bar{\Lambda}K_S^0$ residuals	
Pair System	$\lambda$ value	Pair System	$\lambda$ value	Pair System	$\lambda$ value	Pair System	$\lambda$ value	Pair System	$\lambda$ value	Pair System	$\lambda$ value
3 Residuals (Max Parent $c\tau_{\text{decay}} = 10$ fm)											
AK <sup>+</sup>	0.527	$\bar{\Lambda}K^-$	0.526	AK <sup>-</sup>	0.526	$\bar{\Lambda}K^+$	0.527	AK <sub>S</sub> <sup>0</sup>	0.543	$\bar{\Lambda}K_S^0$	0.544
$\Sigma^0 K^+$	0.111	$\bar{\Sigma}^0 K^-$	0.110	$\Sigma^0 K^-$	0.110	$\bar{\Sigma}^0 K^+$	0.111	$\Sigma^0 K_S^0$	0.120	$\bar{\Sigma}^0 K_S^0$	0.120
$\Xi^0 K^+$	0.039	$\bar{\Xi}^0 K^-$	0.035	$\Xi^0 K^-$	0.038	$\bar{\Xi}^0 K^+$	0.036	$\Xi^0 K_S^0$	0.042	$\bar{\Xi}^0 K_S^0$	0.039
$\Xi^- K^+$	0.050	$\bar{\Xi}^+ K^-$	0.046	$\Xi^- K^-$	0.050	$\bar{\Xi}^+ K^+$	0.046	$\Xi^- K_S^0$	0.054	$\bar{\Xi}^+ K_S^0$	0.050
Other	0.226	Other	0.235	Other	0.228	Other	0.233	Other	0.194	Other	0.199
Fakes	0.048	Fakes	0.048	Fakes	0.048	Fakes	0.048	Fakes	0.048	Fakes	0.048
10 Residuals (Max Parent $c\tau_{\text{decay}} = 4$ fm)											
AK <sup>+</sup>	0.180	$\bar{\Lambda}K^-$	0.180	AK <sup>-</sup>	0.179	$\bar{\Lambda}K^+$	0.181	AK <sub>S</sub> <sup>0</sup>	0.192	$\bar{\Lambda}K_S^0$	0.193
$\Sigma^0 K^+$	0.116	$\bar{\Sigma}^0 K^-$	0.114	$\Sigma^0 K^-$	0.115	$\bar{\Sigma}^0 K^+$	0.116	$\Sigma^0 K_S^0$	0.125	$\bar{\Sigma}^0 K_S^0$	0.124
$\Xi^0 K^+$	0.040	$\bar{\Xi}^0 K^-$	0.037	$\Xi^0 K^-$	0.040	$\bar{\Xi}^0 K^+$	0.037	$\Xi^0 K_S^0$	0.043	$\bar{\Xi}^0 K_S^0$	0.040
$\Xi^- K^+$	0.052	$\bar{\Xi}^+ K^-$	0.047	$\Xi^- K^-$	0.052	$\bar{\Xi}^+ K^+$	0.048	$\Xi^- K_S^0$	0.056	$\bar{\Xi}^+ K_S^0$	0.052
$\Sigma^{*+} K^+$	0.054	$\bar{\Sigma}^{*-} K^-$	0.051	$\Sigma^{*+} K^-$	0.053	$\bar{\Sigma}^{*-} K^+$	0.051	$\Sigma^{*+} K_S^0$	0.058	$\bar{\Sigma}^{*-} K_S^0$	0.055
$\Sigma^{*-} K^+$	0.048	$\bar{\Sigma}^{*+} K^-$	0.050	$\Sigma^{*-} K^-$	0.048	$\bar{\Sigma}^{*+} K^+$	0.050	$\Sigma^{*-} K_S^0$	0.052	$\bar{\Sigma}^{*+} K_S^0$	0.054
$\Sigma^{*0} K^+$	0.048	$\bar{\Sigma}^{*0} K^-$	0.045	$\Sigma^{*0} K^-$	0.048	$\bar{\Sigma}^{*0} K^+$	0.045	$\Sigma^{*0} K_S^0$	0.052	$\bar{\Sigma}^{*0} K_S^0$	0.048
$\Lambda K^{*0}$	0.046	$\bar{\Lambda} \bar{K}^{*0}$	0.047	$\Lambda \bar{K}^{*0}$	0.046	$\bar{\Lambda} K^{*0}$	0.047	$\Lambda K^{*0}$	0.022	$\bar{\Lambda} K^{*0}$	0.022
$\Sigma^0 K^{*0}$	0.041	$\bar{\Sigma}^0 \bar{K}^{*0}$	0.041	$\Sigma^0 \bar{K}^{*0}$	0.041	$\bar{\Sigma}^0 K^{*0}$	0.041	$\Sigma^0 K^{*0}$	0.019	$\bar{\Sigma}^0 K^{*0}$	0.019
$\Xi^0 K^{*0}$	0.014	$\bar{\Xi}^0 \bar{K}^{*0}$	0.013	$\Xi^0 \bar{K}^{*0}$	0.014	$\bar{\Xi}^0 K^{*0}$	0.013	$\Xi^0 K^{*0}$	0.007	$\bar{\Xi}^0 K^{*0}$	0.006
$\Xi^- K^{*0}$	0.018	$\bar{\Xi}^+ \bar{K}^{*0}$	0.017	$\Xi^- \bar{K}^{*0}$	0.018	$\bar{\Xi}^+ K^{*0}$	0.017	$\Xi^- K^{*0}$	0.009	$\bar{\Xi}^+ K^{*0}$	0.008
Other	0.295	Other	0.310	Other	0.299	Other	0.307	Other	0.318	Other	0.330
Fakes	0.048	Fakes	0.048	Fakes	0.048	Fakes	0.048	Fakes	0.048	Fakes	0.048

Table A.1:  $\lambda$  values for the individual components of the AK correlation functions for the case of 3 and 10 residual contributions.

## 626 B Stavinskiy Reference Method

627 Another option for obtaining the reference distribution,  $B(k^*)$ , is to use, what we will refer to as, the  
 628 “Stavinskiy method” [21]. The method was first proposed to handle the case of one event femtoscopy, and  
 629 has been suggested for use in eliminating momentum conservation effects in the reference distribution  
 630 [1]. The method is appropriate for collisions between symmetric projectiles, at sufficiently large energy,  
 631 with a detector which is symmetrical with respect to the transition  $\mathbf{r} \rightarrow -\mathbf{r}$ . The purpose of our use  
 632 of the Stavinskiy method is to rid the correlation functions of the non-femtoscopic background. More  
 633 specifically, our intent is to handle background contributions from elliptic flow, and other sources having  
 634 reflection symmetry in the transverse plane. With the Stavinskiy method, mixed-event pairs are not used  
 635 for the reference distribution; instead, same-event pseudo-pairs, formed by rotating one particle in a real  
 636 pair by  $180^\circ$  in the transverse plane, are used. This rotation rids the pairs of any femtoscopic correlation,  
 637 while maintaining correlations due to elliptic flow (and other suitably symmetric contributors).

638 The results of correctly implementing such a procedure are shown in Figure B.1. The figure shows  
 639 the Stavinskiy method does a very good job of ridding the  $\Lambda K^\pm$  correlations of their non-femtoscopic  
 640 backgrounds. We also see the procedure does not work as well on the  $\Lambda K_S^0$  system.



**Fig. B.1:**  $\Lambda K^+(\bar{\Lambda} K^-)$  correlation functions built using the Stavinskiy method for 0-10%, 10-30%, and 30-50% centralities. Closed symbols represent correlations built using the normal mixed-event reference distribution, while open symbols represent correlations formed using the Stavinskiy same-event pseudo-pairs as a reference.

641 Now, one must be somewhat careful when applying this Stavinskiy method. We found that, in order to  
 642 obtain correct results, we had to run our pseudo-pairs through the same pair cuts used in our analyses. In  
 643 an ideal world, our pair cut would only remove truly bad pairs from splitting, merging, etc. In the  
 644 real world, the pair cut always throws out some of the good with the bad. For the pseudo-pairs to form a  
 645 reliable reference, they too must experience the pair cut, and the loss of “good” pseudo-pairs. We found  
 646 this issue affected mainly our  $\Lambda K^+$  &  $\bar{\Lambda} K^-$  analysis.

647 **C Strong and Coulomb Fitter**

648 When modeling systems which include both strong and Coulomb effects, Eq. 10 is no longer valid, and,  
 649 in fact, there is no analytical form with which to fit. To solve such a problem, and to fit such a system, one  
 650 must develop a more fundamental model, beginning with Eq. 4 and using the two-particle wave-function  
 651 including both strong and Coulomb interactions [22]:

$$\Psi_{\mathbf{k}^*}(\mathbf{r}^*) = e^{i\delta_c} \sqrt{A_c(\eta)} [e^{i\mathbf{k}^*\cdot\mathbf{r}^*} F(-i\eta, 1, i\xi) + f_c(k^*) \frac{\tilde{G}(\rho, \eta)}{r^*}] \quad (\text{C.1})$$

652 where  $\rho = k^* r^*$ ,  $\eta = (k^* a_c)^{-1}$ ,  $\xi = \mathbf{k}^* \cdot \mathbf{r}^* + k^* r^* \equiv \rho(1 + \cos \theta^*)$ , and  $a_c = (\mu z_1 z_2 e^2)^{-1}$  is the two-  
 653 particle Bohr radius (including the sign of the interaction).  $\delta_c$  is the Coulomb s-wave phase shift,  $A_c(\eta)$   
 654 is the Coulomb penetration factor,  $\tilde{G} = \sqrt{A_c}(G_0 + iF_0)$  is a combination of the regular ( $F_0$ ) and singular  
 655 ( $G_0$ ) s-wave Coulomb functions.  $f_c(k^*)$  is the s-wave scattering amplitude:

$$f_c(k^*) = [\frac{1}{f_0} + \frac{1}{2} d_0 k^{*2} - \frac{2}{a_c} h(\eta) - ik^* A_c(\eta)]^{-1} \quad (\text{C.2})$$

656 where, the “h-function”,  $h(\eta)$ , is expressed through the digamma function,  $\psi(z) = \Gamma'(z)/\Gamma(z)$  as:

$$h(\eta) = 0.5[\psi(i\eta) + \psi(-i\eta) - \ln(\eta^2)] \quad (\text{C.3})$$

657 In this case, the  $\lambda$  parameter may be included as:

$$C(\mathbf{k}^*) = (1 - \lambda) + \lambda \int S(\mathbf{r}^*) |\Psi_{\mathbf{k}^*}^S(\mathbf{r}^*)|^2 d^3 \mathbf{r}^* \quad (\text{C.4})$$

658 To build a fit function for a system including both strong and Coulomb interactions we considered two  
 659 related options. The first option was to numerically integrate Eq.4. The second option was to simulate  
 660 a large sample of particle pairs, calculate the wave function describing the interaction, and average to  
 661 obtain the integral in Eq.4. In either case, the solution would involve some very complicated mathemat-  
 662 ical functions, as can be seen in Eqs. C.1 to C.3. Having no experience with either of these options, we  
 663 elected the latter of simulating pairs.

664 **D Spherical Harmonic Decomposition**

665 In Fig. D.1 we show results for the  $C_{00}$  and  $\Re C_{11}$  components from the spherical decomposition of our  
 666  $\Lambda K^+$  system in the 0-10% centrality bin. As seen in the figure, the  $C_{00}$  signal is similar to that observed  
 667 in our one-dimensional study. The  $\Re C_{11}$  component shows a clear deviation from zero, and the negative  
 668 value signifies that the  $\Lambda$  particles are, on average, emitted further out and/or earlier than the  $K$  mesons.

669 **E Relative Emission Shifts with THERMINATOR 2**

670 Fig. E.1 shows results from the THERMINATOR 2 event generator for an impact parameter of  $b = 2$  fm.  
 671 As THERMINATOR does not include any final state effects, the femtoscopic correlation was introduced  
 672 by assuming a set of scattering parameters  $(\Re f_0, \Im f_0, d_0) = (-1.16, 0.51, 1.08)$  and weighting the signal  
 673 distribution (numerator pairs) with the modulus squared of the two-particle wave function,  $|\Psi|^2$ .

674 The top left of Fig. E.1(a) shows a fit to the one-dimensional correlation function from THERMINA-  
 675 TOR 2. The scattering parameters are known precisely here, as they served as the weights used in the  
 676 simulation, and are kept constant in the fit. We are interested in looking at the extracted one-dimensional

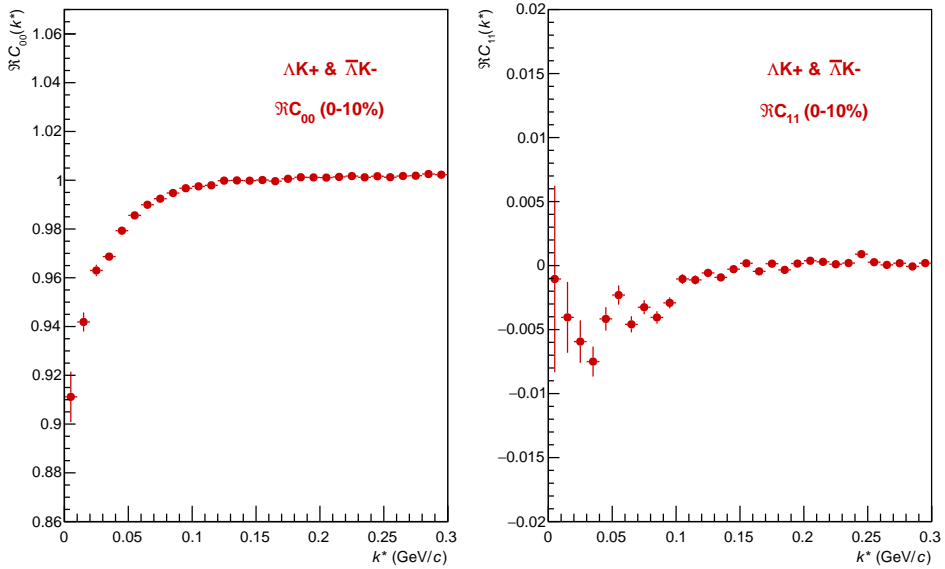
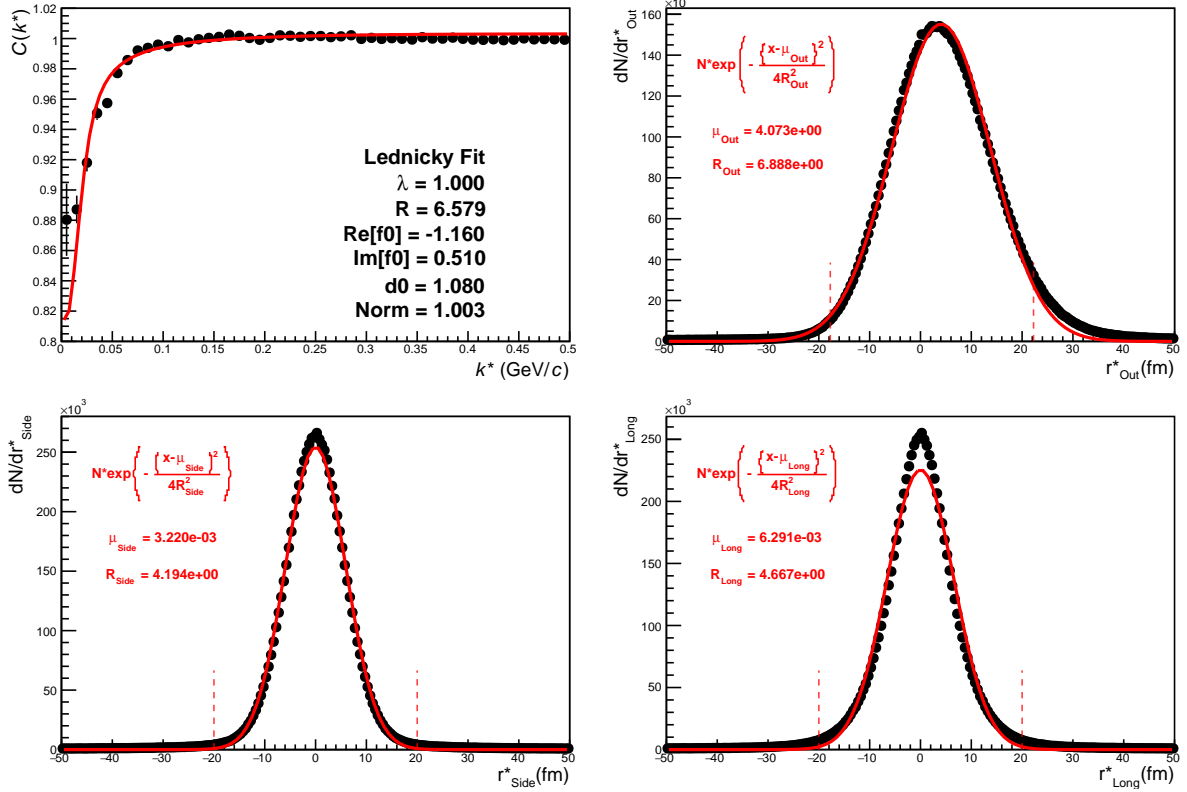


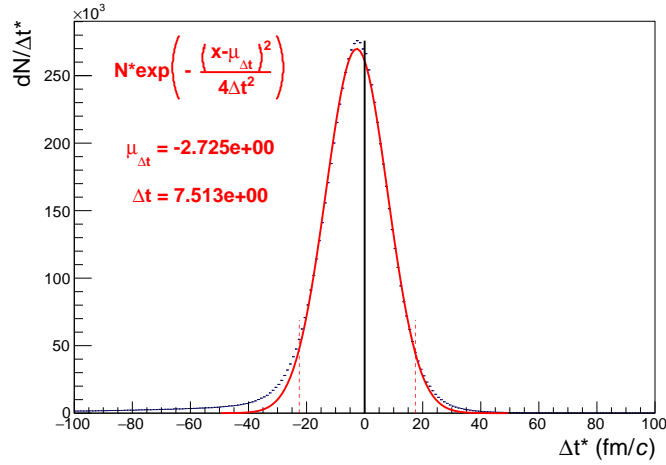
**Fig. D.1:**  $C_{00}$  (left) and  $\Re C_{11}$  (right) components of a spherical harmonic decomposition of the  $\Lambda K^+$  correlation function for the 0-10% centrality bin. The  $C_{00}$  component is similar to the 1D correlation functions typically studied, and probes the overall size of the source. The  $\Re C_{11}$  component probes the asymmetry in the system; a non-zero value reveals the asymmetry

677 source size here, so the  $\lambda$  parameter is also fixed at unity. The other three plots in Fig. E.1(a) show the  
 678 source distribution in the out (top right), side (bottom left), and long (bottom right) directions (all in the  
 679 PRF). The source distributions have all been fitted with a Gaussian form, the result of which is printed  
 680 within the respective plot. One immediately sees a significant shift in the out direction,  $\mu_{\text{out}} \approx 4$  fm, and  
 681 negligible shift in the other two directions,  $\mu_{\text{side}} \approx \mu_{\text{long}} \approx 0$  fm. The figure demonstrates that, within  
 682 the THERMINATOR 2 model, the  $\Lambda$  is, on average, emitted further out than its  $K$  partner. Finally, Fig.  
 683 E.1(b) shows the distribution of the relative time of emittance, again in the PRF. The figure shows that  
 684 the  $\Lambda$  is, on average, emitted earlier than its  $K$  partner.

685 We end this section with a brief look at how a spatial separation of the single particle sources affects  
 686 the radii extracted from a femtoscopic analysis. To achieve this, we use THERMINATOR 2 in a similar  
 687 fashion as described above, but with one important difference. Instead of taking the source information  
 688 from THERMINATOR 2, we instead draw the source from a pre-determined Gaussian distribution. In  
 689 all cases, we take  $R_{\text{out}} = R_{\text{side}} = R_{\text{long}} = 5$  fm, and  $\mu_{\text{side}} = \mu_{\text{long}} = 0$  fm. In Figure E.2, we show results  
 690 for the case of  $\mu_{\text{out}} = 1$  fm,  $\mu_{\text{out}} = 3$  fm, and  $\mu_{\text{out}} = 6$  fm. In this figure, we do not show the side and  
 691 long distributions, as they are simple Gaussians of width 5 fm centered about the origin. The figure  
 692 demonstrates that as the separation  $\mu_{\text{out}}$  increases, so do the extracted femtoscopic radii.



(a) (Top Left) Simple fit on simulation from THERMINATOR 2. Generated source in the (Top Right) out, (Bottom Left) side, and (Bottom Right) long directions.



(b) Temporal characteristics of the source.

**Fig. E.1:** Extracted radius when performing a simple fit on simulation from THERMINATOR 2, along with the spatio-temporal characteristics generated by the simulation.

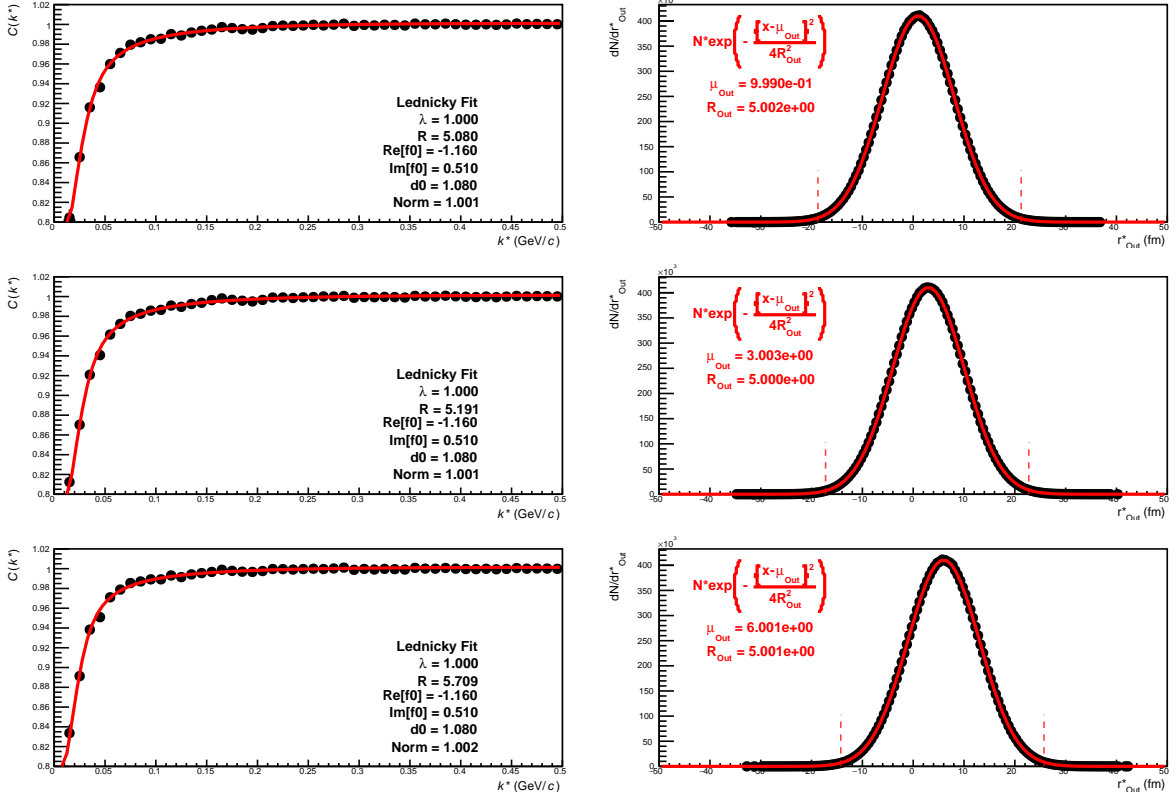


**Fig. E.2:** Probing the effect of varying the source shift in the outward direction,  $\mu_{\text{Out}}$ , within the THERMINATOR 2 framework. To achieve this, we formed particle pairs from the simulation, but altered their spatial characteristics by drawing the out, side, and long components from pre-determined Gaussian distributions. The plots on the left show fits resulting from the sources (in the out direction) shown on the right. The sources in the side and long directions are not shown, and are both Gaussians of width 5 fm centered at the origin for all cases. Moving from top to bottom,  $\mu_{\text{Out}}$  increase from 0 to 6 fm, the effect of which clearly increases the effective radius extracted in the fit.

693 **F The ALICE Collaboration**